Observation and modelling of atmospheric OH and HO_2* radicals at a subtropical rural site and implications for secondary pollutants

Zhouxing Zou[1#], Tianshu Chen[1#], Qianjie Chen[1], Weihang Sun[1], Shichun Han[1], Zhuoyue Ren[2], Xinyi Li[2], Wei Song[2], Aoqi Ge[2], Qi Wang[2], Xiao Tian[2], Chenglei Pei[3], Xinming Wang[2], Yanli Zhang[2], and Tao Wang[1]

[#] These authors contributed equally to this work

[1] Department of Civil and Environmental Engineering, The Hong Kong Polytechnic University, Hong Kong, China

[2] Guangzhou Institute of Geochemistry, Chinese Academy of Sciences, Guangzhou, China

[3]Guangdong Province Guangzhou Ecological Environment Monitoring Center Station, Guangzhou 510030, China.

Correspondence to: Tao Wang (tao.wang@polyu.edu.hk)

Abstract

HO_X radicals (OH and HO_2) are crucial oxidants that determine atmospheric oxidation capacity and the production of secondary pollutants; however, their sources and sinks remain incompletely understood in certain rural, forest and maritime environments. This study measured HO_2* (HO_2 + parts of RO_2) and OH concentrations using a chemical ionisation mass spectrometer at a subtropical rural site in southern China from 12 November to 19 December 2022. The average peak concentrations were 3.50 ± 2.47 × 10^6 cm^{-3} for OH and 1.34 ± 0.93 × 10^8 cm^{-3} for HO_2*. Model estimated interference to HO_2 by RO_2 possibly contributed to 44%-69% of the HO_2*. Calculations based on an observation-constrained chemical model revealed an overestimation of HO_2 and OH concentrations during warm periods of the field study. Sensitivity tests suggest that adding HO_x sinks or a HO_2 recycle process to the model could improve the model performance. Over-simulation of HO_x in the model resulted in overestimations of midday production rates by more than 79% for ozone and a factor of 1.88 for nitric acid.

Our study highlights the need for further improving understanding of the sources/sinks of OH and HO_2 and representation of them in air quality models.

1. Introduction

The HO_X family, comprising hydroxyl (OH) and peroxy radicals (HO_2), plays a pivotal role in the Earth's atmosphere by driving photochemical processes that influence the air composition and chemistry. OH radicals are primarily produced by the photolysis of ozone (O_3), nitrous acid (HONO), and ozonolysis of alkenes. They initiate the oxidation of CO and most volatile organic compounds (VOCs), producing HO_2 and other peroxyl radicals (RO_2, where R represents an alkyl group). HO_2 is also generated from the photolysis of oxygenated VOCs (OVOCs) and by reactions between OVOCs and OH. In the presence of NO, RO_2 radicals are converted to HO_2 and then to OH radicals, buffering OH concentrations and maintaining atmospheric oxidation capacity. (Stone et al., 2012). These interactions are crucial in the formation of photochemical smog and secondary organic aerosol (SOA), which generate NO_2, O_3, and highly oxygenated molecules. HO_X radicals are removed through reactions of OH with inorganic trace gases, self-reactions among radicals, peroxyacetyl nitrate (PAN) formation, and the heterogeneous uptake by aerosols. These processes subsequently contribute to atmospheric acidification and aerosol formation through the production of H_2SO_4 and HNO_3. See Figure S1 and Table S1 for detailed processes and chemical reactions.

The accuracy of model-predicted OH is a crucial indicator for assessing our understanding of atmosphere processes (Heard and Pilling, 2003). There is a longstanding debate regarding the discrepancies between simulated and observed radical concentrations under low NO_x conditions, which remains a significant issue (Hofzumahaus et al., 2009; Stone et al., 2012; Zou et al., 2023). Previous studies have shown that models generally predict OH levels well in polluted conditions (NO > 1 ppb), but notable overestimations were observed under low NO and aged conditions, such as coastal areas (Kanaya et al., 2007; Zou et al., 2023), marine boundary layers (Berresheim et al., 2002; Carslaw et al., 1999), and the rural area (Bottorff et al., 2023;

Kanaya et al., 2012). Missing OH sinks from both measurement and chemical mechanism were proposed as the primary reason for the overestimation (Lou et al., 2010; Yang et al., 2016; Hansen et al., 2014; Thames et al., 2020). Underestimations of OH concentrations were also observed in high biogenic VOCs (BVOCs) and low NO (<1 ppb) conditions which generally happen in the subtropical or tropical area (Hofzumahaus et al., 2009; Lelieveld et al., 2008; Tan et al., 2001; Whalley et al., 2011). After considering a new OH regeneration mechanism (Wennberg et al., 2018; Novelli et al., 2020) and measurement interference (Feiner et al., 2016; Hens et al., 2014; Mao et al., 2012; Novelli et al., 2014; Woodward-Massey et al., 2020), daytime OH concentrations could be reasonably reproduced by the model in the high BVOC conditions, with some unresolved underestimation in the evening (Jeong et al., 2022; Lew et al., 2020; Tan et al., 2019). Those results call for more measurement and modelling in subtropical and tropical rural areas.

HO_2 concentrations were consistently underpredicted in the polluted urban sites (Ma et al., 2019; Yang et al., 2021; Ma et al., 2022) , with no clear trends in relatively clean regions. Some studies reported good agreement between measurement and model prediction (Feiner et al., 2016; Lew et al., 2020), whereas others indicated model overprediction (Bottorff et al., 2023; Griffith et al., 2013) and underprediction (Whalley et al., 2010; Kim et al., 2013; Mallik et al., 2018; Tan et al., 2017;). These discrepancies may be attributed to several factors, including measurement interference caused by RO_2 recycling in environments rich in BVOCs or aromatics (Fuchs et al., 2011), uncertainties associated with heterogeneous uptake in box models (Yang et al., 2022), and the outflow (or entrainment) of reservoir species like PAN (Griffith et al., 2013) (Whalley et al., 2010) . Despite these advances, it remains difficult to pin down the exact causes of the model-measurement discrepancies in some of the previous studies.

In the present study, we measured concentrations of OH and HO_2* using a quadrupole chemical ionization mass spectrometer (PolyU-CIMS) from November to December 2022 at a subtropical rural site in southern China. We tested model's capability in reproducing the radical concentrations and elucidate factors contributing

to discrepancy under varying temperatures, VOCs, and NO_X conditions. The Methodology section describes the measurement site, the principles and the configuration of PolyU-CIMS, and the setup of chemical box models. The Results and Discussion section details our findings, providing an analysis of the radical concentrations and exploring the discrepancies between observed data and model predictions. By employing an observation-constrained box model, we analyzed the radical budgets and investigated potential causes for these discrepancies. The study concludes with a discussion of the implications of these findings.

2. Methodology

2.1 Measurement Site

The field campaign was conducted at the Conghua Liangkou Air Monitoring Station (23°44'47"N, 113°47'06"E, 200m, above sea level) from November 12 to December 19, 2022 (Figure 1). The site is located at the northern part of the Pearl River Delta (PRD), approximately 80 kilometers from the densely populated areas. It is nestled within the Liuxi River National Forest Park (an evergreen broad-leaf forest). The site is situated just north of the G105 national highway and around 0.5 kilometers east of Liangkou town. Even though it is close to the road, the traffic was generally limited during the observation period due to the coronavirus disease pandemic (COVID-19). The site is subject to BVOCs emission, predominantly isoprene, from the surrounding forest when the daytime temperatures exceeds 20°C, and NO emissions from the nearby national highway, particularly during periods of low wind speeds. The measurements included trace gases such as O_3, NO, NO_2, CO, HONO, VOCs, OVOCs, meteorological data such as relative humidity (RH), temperature, and photolysis frequencies of HONO, NO_2, O_3, H_2O_2, and HCHO. Details about the instruments are shown in Table S2.

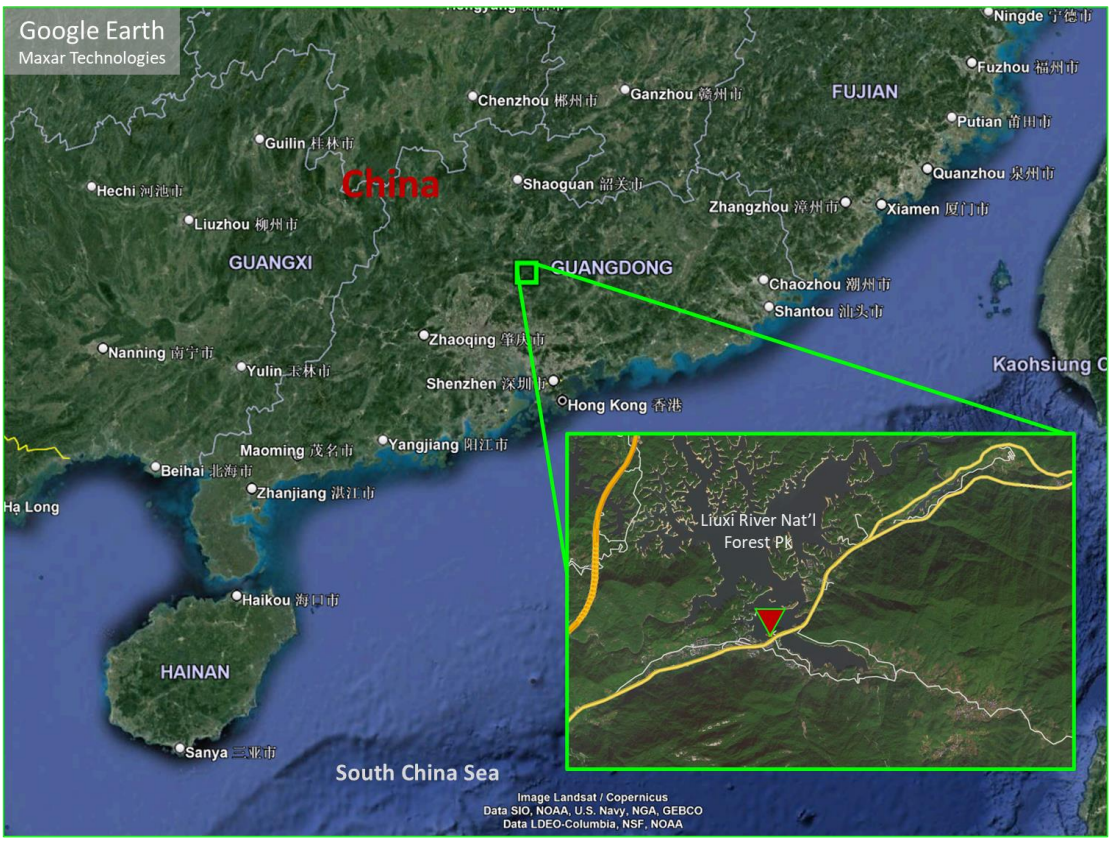

Figure 1 Geographic location of the measurement site (Liangkou Air Monitoring station 23°44'47"N, 113°47'06"E, 200 m a.s.l. marked by the red inverted triangle) in Conghua, Guangdong Province, South China. The map is sourced from © Google Earth and © Amap.

2.2 Radical measurement principle

OH and HO_2 radicals were measured using the Hong Kong Polytechnic University's quadrupole Chemical Ionization Mass Spectrometer (PolyU-CIMS), which had been used in a previous study for OH measurement (Zou et al., 2023). The use of CIMS for OH measurement was pioneered by Eisele and Tanner (1991), with subsequent enhancements in measurement accuracy (Eisele and Tanner, 1993; Tanner et al., 1997; Tanner and Eisele, 1995) and the adoption of inlets for simultaneous measurements of HO_2 and RO_2 (Edwards et al., 2003; Sjostedt et al., 2007), H_2SO_4 (Mauldin III et al., 2004), and OH reactivity (Muller et al., 2018).

Figure 2 illustrates the measurement principle of the PolyU-CIMS used in this campaign. Briefly, the ambient OH radicals are converted to H_2SO_4 in the sample inlet system by reacting with SO_2 (R21 in the reaction Table S1). These are then transformed to HSO_4^- ion clusters in the ionization chamber by the reactions with a reagent gas in

sheath flow (HNO_3, R24 to 27), and ultimately dissociated (R29) for detection by the mass spectrometer system at m/z 97 (S_{97SO2} in Figure 2). To mitigate interference and noise, scavenger gases (C_3F_6 in this study) were introduced to scavenge the ambient OH, creating a background signal (R23, $S_{97ScaSO2}$ in Figure 2). See Text S3 in the Supplementary Information for details about the scavenging efficiency. The ambient OH radicals signal (S_{OH}) is then determined by subtracting $S_{97ScaSO2}$ from S_{97SO2}. The OH concentration is calculated using the following equation:

$$[OH] = \frac{1}{C_{OH}} \times \frac{S_{OH}}{S_{62}} \quad \text{(E1)}$$

Where C_{OH} represents the calibration factors of OH, and S_{62} is the signal corresponding to the reagent ion (NO_3^-). The detailed calibration procedure for OH is outlined in previous studies (Kürten et al., 2012; Zou et al., 2023) and also in Text S1. Ambient and injected NO can interfere with OH measurements through reaction of NO + HO_2. The interference by ambient NO is estimated using a model (within a range of 10^4 – 10^5 cm^{-3}) and was subtracted from the ambient OH measurements (see Text S4.2). The interference from the injected NO after HO_2 measurement is discussed in Text S4.2 and is mitigated through the duty cycle configuration described in Text S5.

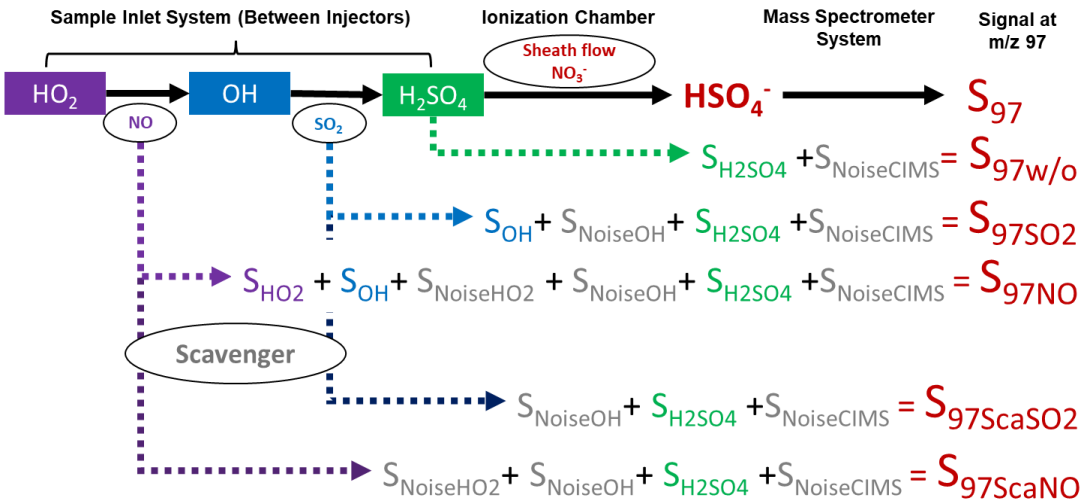

Figure 2 Flow chart depicts the relationship between measurement species and signal intensity at m/z 97 (S_{97}) with various gas injections. The color-filled grids label the ambient species, while oval shapes label the species injected into the sample flow. Signal intensities with different gas additions to the sample flow are represented by $S_{97w/o}$, S_{97SO2}, S_{97NO}, $S_{97ScaSO2}$, and $S_{97ScaNO}$. The signals correspond to ambient OH, HO_2, H_2SO_4 and noise from OH measurement, HO_2 measurement and the CIMS denoted as S_{OH}, S_{HO2}, S_{H2SO4}, $S_{NoiseOH}$, $S_{NoiseHO2}$, and $S_{NoiseCIMS}$, respectively.

To measure ambient HO_2, NO is injected into the sample flow, converting HO_2 to OH (R11). This converted OH then follows the same reaction pathway (R21, R24 through R27, and R29) and is measured at m/z 97 (S_{97NO} in Figure 2). Similar to the OH measurement, the background signal for HO_2 ($S_{97ScaNO}$ in Figure 2) is determined by introducing the scavenger gas. The corresponding signal for ambient HO_2 (S_{HO2}, as shown in Figure 2) is determined by subtracting $S_{97ScaNO}$ and S_{OH} from S_{97NO}. The HO_2 concentration is calculated using an equation similar to E1, by replacing S_{OH}, and C_{OH} to S_{HO2} and C_{HO2}, respectively (E2).

$$[HO_2] = \frac{1}{C_{HO2}} \times \frac{S_{HO2}}{S_{62}} \quad \text{(E2)}$$

The procedure for determining the HO_2 calibration factor, C_{HO2}, is akin to that for C_{OH} (Text S1). The calibration tube generates equal amounts of radicals (R30 in SI, $[OH]/[HO_2] = 1$), allowing for simultaneous calibration of HO_2 and OH with and without NO addition to the sample flow.

In addition to HO_2, the added NO can also react with RO_2 and produce HO_2, which is a potential interference leading to an overestimation of ambient HO_2 levels (Edwards et al., 2003; Hanke et al., 2002; Fuchs et al., 2011; Whalley et al., 2013; Fuchs et al., 2014). For our CIMS configuration, the model estimated daytime interference increased HO_2 by 79% to 222% ($[RO_2 \text{ interference}]/[HO_2] \times 100\%$) during the field study (Text S4.3 and Figure S9). Considering the uncertainties of RO_2 mechanisms in the MCM model, we opted not to use model results to correct RO_2 interference and denote our HO_2 measurement hereafter as HO_2* which is the maximum value of the ambient HO_2 concentrations.

Compared to the configuration of PolyU-CIMS in the previous campaign (Zou et al., 2023), the instrument has been upgraded for simultaneous HO_2* measurements. Refer to Figure S2 and Text S2 for modification to HO_2* measurement and to Text S5 for measurement duty cycle. Apart from these modifications, the settings and configurations of the PolyU-CIMS remained the same as those in the previous campaign (see Table S3). With the updated configuration, the PolyU-CIMS achieved the simultaneous measurement of OH, HO_2*, and H_2SO_4.

The calibration factors, detection limits and accuracies were 1.09×10^{-8} cm^{-3}, 3×10^{5} cm^{-3}, and 44% for OH; 6.01×10^{-9} cm^{-3}, 2×10^{6} cm^{-3}, and 46% for HO_2*; and 1.09×10^{-8} cm^{-3}, 1×10^{5} cm^{-3}, and 40% for H_2SO_4, respectively (Table S3).

2.3 Box Model

HO_X concentrations in this study were simulated using the Framework for 0-D Atmospheric Modelling (F0AM, Wolfe et al., 2016) with the Master Chemical Mechanism (MCM) v3.3.1 (http://mcm.leeds.ac.uk/MCM), which encompasses over 6,700 species and 17,000 reactions. MCM v3.3.1 features a near-explicit chemical mechanism that includes isoprene degradation and OH regeneration mechanisms. This mechanism has previously been employed to investigate HO_X chemistry and conducting budget analyses (Slater et al., 2020; Tan et al., 2018; Zou et al., 2023). The gas-phase chlorine chemistry described by Xu et al. (2015) and Wang et al. (2019) was included in the model (Chen et al., 2022).

In the baseline scenario, the observation data were aggregated into one-hour intervals to provide input for the model, initially constraining it without incorporating observed OH and HO_2* data. For the assessment of ozone formation rates, the model was adjusted to include constraints based on the actual measured concentrations of OH and HO_2*. Observed VOCs were categorized into anthropogenic origin (AVOCs), including species from petroleum gas and industrial solvent evaporation (alkenes, alkenes, benzene, and TEXs - toluene, ethylbenzene, and xylenes), and OVOCs comprising aldehydes, ketones, and acids. The sole BVOC measured in this study was isoprene. Methacrolein (MACR), a derivative of isoprene, is distinctly classified among the biogenically sourced OVOCs for further discussion. Physical processes like deposition and entrainment in the model were represented by a first-order physical loss with a 24-hour lifetime for all species (Chen et al., 2022; Wolfe et al., 2016; Zou et al., 2023). The model also included the heterogeneous uptake of HO_2 by aerosols, represented as a pseudo-first order loss (Jacob, 2000):

$$\frac{d[HO_2]}{dt} = -k_{HO_2}[HO_2] \quad \text{(E3)}$$

$$k_{HO_2} = \frac{V_{HO_2} \times S_a \times \gamma_{HO_2}}{4} \quad \text{(E4)}$$

$$v_{HO_2} = \sqrt{\frac{8RT}{\pi \times M_{HO_2}}} \quad \text{(E5)}$$

Here, k_{HO_2} represents the first-order loss rate coefficient of HO_2 by aerosol uptake, determined by the effective HO_2 uptake coefficient γ_{HO2} (0.1, Guo et al., 2019), the mean molecular velocity of HO_2 (v_{HO_2}), the aerosol surface area concentration (S_a) measured by the Scanning Mobility Particle Sizing (SMPS); and the molecular mass of HO_2 (M_{HO_2} = 17 g/mol). As aerosol and aqueous phase chemistry were not included in the model, it was assumed that the heterogeneous HO_2 loss would not lead to further reactions (Guo et al., 2019). For each day, a three-day spin-up was performed with constant inputs to establish stable model chemistry and reduce the uncertainty of unconstrained species. Refer to Text S4 for details on model setup for interferences assessment.

3. Results and Discussion

3.1 Results from Observations

3.1.1 Overview

Figure 3 illustrates a time series showing observed concentrations of radical and trace gases, along with meteorological parameters, from 12 November to 19 December 2022. In November, the conditions were characterised by warm temperatures ranging from 29°C to 19°C and high relative humidity averaging 86%. In contrast, December witnessed a significant decrease in temperature (ranging from 20°C to 9°C) and a reduction in relative humidity (averaging 72%). Wind speeds during the campaign were generally low, averaging 0.9 ± 0.6 m/s and typically remaining below 3.0 m/s, with higher speeds occurring towards the end of December. In November, daytime winds predominantly blew from the south, while nighttime winds came from the north. In December, northerly winds predominated both day and night. Detailed hourly wind speed and direction data are illustrated in Figure 3, and wind roses are shown in Figure S3. On days with low wind speeds (less than 0.5 m/s), NO_X emissions from the G105 national highway significantly influenced chemical measurements at the monitoring site, causing morning NO levels to peak at several parts per billion (ppb). Isoprene

concentrations peaked in the afternoons, ranging from 0.2 to 1.7 ppb in November and dropping to less than 0.1 ppb in December. Other trace gases and particulate matter levels were higher in November than in December.

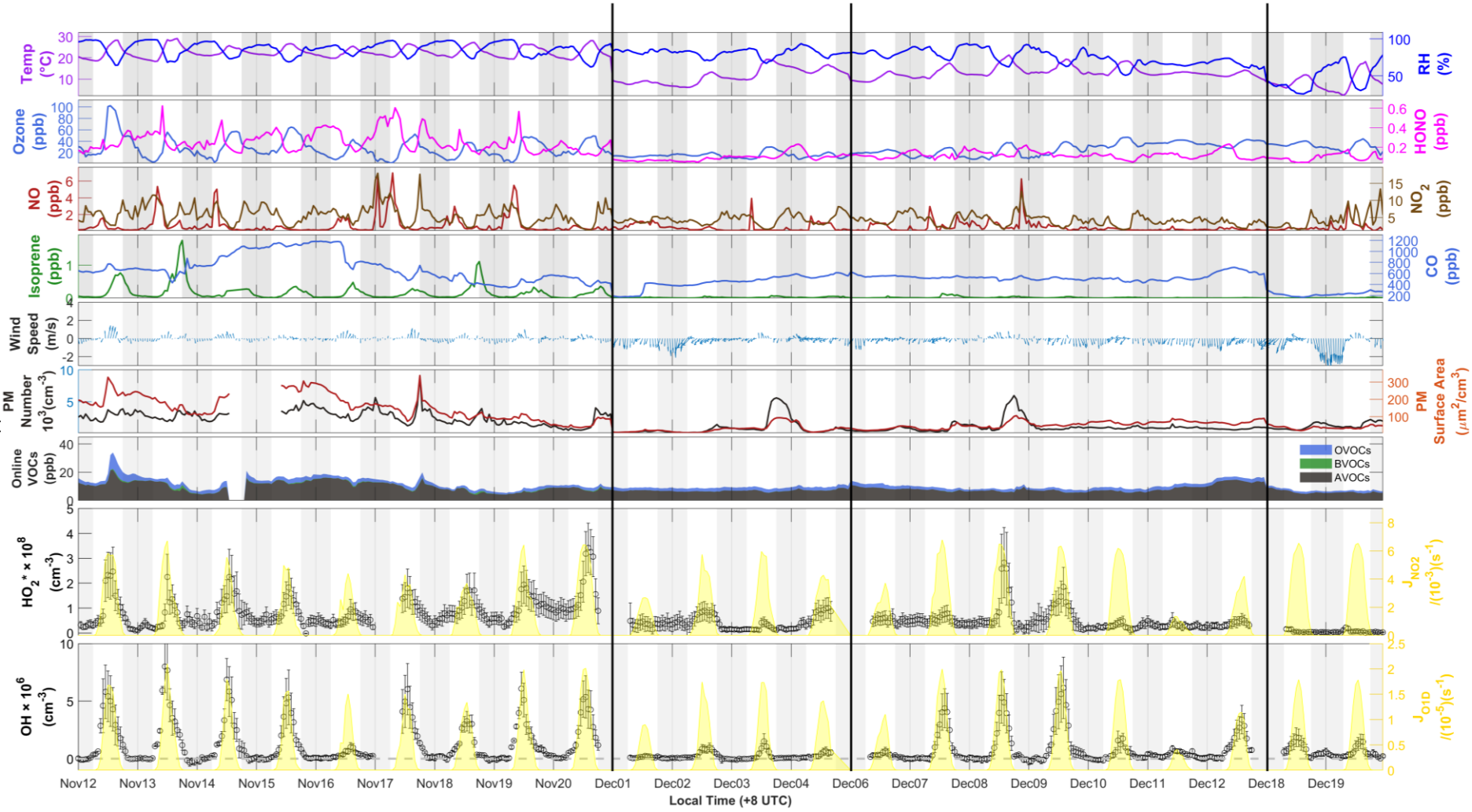
Temp (°C)
RH (%)
Ozone (ppb)
HONO (ppb)
NO (ppb)
NO2 (ppb)
Isoprene (ppb)
CO (ppb)
Wind Speed (m/s)
PM Number 10^3(cm^-3)
PM Surface Area (μm^2/cm^3)
Online VOCs (ppb)
OVOCs
BVOCs
AVOCs
HO2* × 10^8 (cm^-3)
J_NO2 /(10^-3)(s^-1)
OH × 10^6 (cm^-3)
J_O1D /(10^-5)(s^-1)
Nov12
Nov13
Nov14
Nov15
Nov16
Nov17
Nov18
Nov19
Nov20
Dec01
Dec02
Dec03
Dec04
Dec06
Dec07
Dec08
Dec09
Dec10
Dec11
Dec12
Dec18
Dec19
Local Time (+8 UTC)

Figure 3 Time series of HO_2* and OH radicals from 12 November to 19 December, showing measured weather conditions (temperature, RH, wind speed, and wind direction), primary sources of HO_X radicals (ozone, HONO), important sinks of the radicals (CO, isoprene, and VOCs), and photolysis frequencies of NO_2 (J_{NO2}) and ozone (J_{O1D}). Non-continuous days during the campaign are delineated by a black line. The PRD, CEC, and CNC periods for further analysis were labelled in red, orange, and blue, respectively. The x-axis is in local time (+8 UTC).

Throughout the campaign, the daytime concentrations of OH and HO_2* consistently exceeded detection limits and showed distinct diurnal patterns. The OH concentrations typically peaked around midday, while the HO_2* levels reached their maximum approximately one to two hours later (Figure S4). The daily maximum concentration of OH varied significantly, ranging from 8.00×10^6 cm^{-3} to nearly the detection limit of 2.54×10^5 cm^{-3}, with an average of $3.50 \pm 2.47 \times 10^6$ cm^{-3} (Table 1). Similarly, the daily maximum concentration of HO_2* varied from 3.42×10^8 cm^{-3} to 2.17×10^7 cm^{-3}, averaging $1.34 \pm 0.93 \times 10^8$ cm^{-3} (Table 1). At nighttime, while the HO_2* levels generally remained above the detection threshold, the OH concentrations frequently approached the threshold. The average nighttime concentrations were 3.92×10^7 cm^{-3} for HO_2* and 1.64×10^5 cm^{-3} for OH. We compared the observed OH and HO_2* concentrations with those reported in previous studies conducted in urban, suburban, rural forest, and coastal sites. As illustrated in Figure S5, the OH concentrations were generally lower than those found in urban settings but similar to levels observed in suburban, rural, and forest environments. This suggests a moderate level of anthropogenic activity typical of mixed rural settings. In contrast, the HO_2* concentrations during these periods were significantly lower than earlier observations in rural and forest environments, likely owing to reduced photochemical activity during our measurement period.

Table 1 Average concentrations and standard deviation of measured species throughout the entire campaign (Total) and the selected 3 days cases from each cluster (PRD, CEC and CNC).

Species (Unit)	Total	PRD	CEC	CNC
AveMax OH_{Obs} 10^6 (cm^{-3})	3.5±2.5	6.9±1.1	4.9±1.5	5.3±0.9
OH_{Obs} 10^6 (cm^{-3})	0.9±1.5	1.6±2.2	1.4±1.6	1.2±1.8
OH_{DL} 10^6 (cm^{-3})	0.5±0.3	0.4±0.3	0.4±0.2	0.9±0.6
AveMax $HO_{2\,Obs}$ 10^8 (cm^{-3})	1.34±0.93	2.32±1.25	2.36±0.92	1.82±1.02
$HO_2{}^*{}_{Obs}$ 10^8 (cm^{-3})	0.59±0.51	0.76±0.63	1.10±0.68	0.67±0.55
$HO_2{}^*{}_{DL}$ 10^8 (cm^{-3})	0.19±0.11	0.17±0.10	0.25±0.08	0.26±0.15
Pressure (hpa)	995±4	992±1	992±1	995±2
Temp (°C)	16±6.1	23±3.0	23±2.6	14±2.8
RH (%)	78±15	87±11	86±10	81±9.4
Wind Speed (m/s)	0.91±0.65	0.53±0.32	0.57±0.34	0.87±0.5
j_{O1D} 10^{-6}(s^{-1})	3.2±5.4	3.5±6	3.6±5.9	4.0±6.6
j_{NO2} 10^{-3} (s^{-1})	1.3±1.9	1.3±2.1	1.4±2	1.6±2.3
HONO	0.169±0.104	0.249±0.084	0.201±0.070	0.133±0.033
SO_2	0.5±0.8	0.5±0.6	0.4±0.5	0.4±0.5
NO_2	4.89±2.37	6.25±2.47	4.84±2.23	4.52±1.97
NO	0.57±0.86	0.73±1.09	0.69±1.00	0.73±0.85
CO	557.36±225.92	739.41±153.84	464.73±74.34	513.36±22.02
Ozone	25±14	32±23	24±13	19±9.4
Particle Surface Area (um^2/cm^3)	86±72	186±51	84±28	48±19
Isoprene	0.082±0.174	0.257±0.337	0.155±0.200	0.029±0.030
*OVOCs	2.218±1.056	3.163±2.324	1.755±0.379	1.730±0.330
*AVOCs	8.346±3.223	9.662±5.031	6.886±1.755	6.801±0.864
*TEXs	0.356±0.316	0.801±0.616	0.266±0.090	0.237±0.085

Notes: Concentrations are expressed in parts per billion (ppb) unless otherwise specified. Total VOCs concentrations are categorized by origin (AVOCs and OVOCs). For the average concentration of each measured VOC, refer to Table S5.

Figure 4 illustrates the results of the 24-hour backward trajectory analysis, revealing three distinct but sequentially occurring phases. In the initial phase (Figure 4a), air masses originated from the urban and industrial zones of the Pearl River Delta (PRD). This phase was characterised by intense photochemical activity, with ambient temperatures exceeding 20°C and relative humidity levels surpassing 70%. During this period, notably high concentrations of VOCs, ozone, and radicals were observed, with the average daily maximum concentrations of OH and HO_2* radicals reaching 6.50 ± 1.19 × 10^6 cm^{-3} and 2.20 ± 0.27 × 10^8 cm^{-3}, respectively. The subsequent phase was characterised by air masses originating from Central East China (CEC, Figure 4b). This phase showed reduced photochemical reactivity and lower concentrations of the measured trace gases. The average daily maximum concentrations of OH and HO_2* during this phase were 4.35 ± 2.19 × 10^6 cm^{-3} and 1.96 ± 0.90 × 10^8 cm^{-3}, respectively.

The final phase was influenced by air masses from Central North China (CNC, Figure 4c), which exhibited the lowest concentrations of trace gases and the least pronounced average daily maximum concentrations in OH and HO_2* concentrations, measured at $2.23 \pm 1.95 \times 10^6$ cm^{-3} and $7.63 \pm 7.66 \times 10^7$ cm^{-3}, respectively. This phase coincided with an increase in cloudy days and a decrease in temperatures, indicating reduced photochemical conditions.

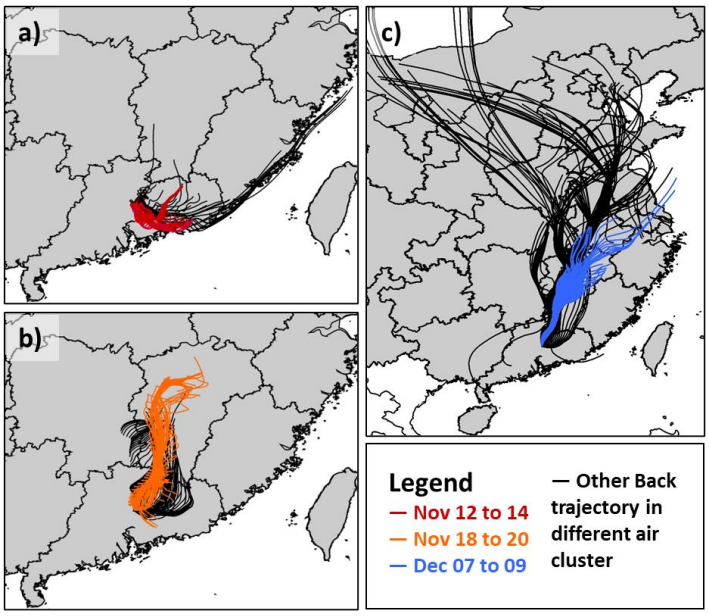

Figure 4 24-hour back trajectories for (a) Pearl River Delta (5 days), (b) Central East China (4 days), and (c) Central North China (14 days) cases. Three days selected from each cluster for model simulation are distinguished by different colours.

3.1.2 Selection of Cases

For each phase, a representative three-day period was selected for detailed analysis based on the availability of comprehensive data and sunny conditions (colored trajectories in Figure 4). In the subsequent analysis, 'PRD,' 'CEC,' and 'CNC' refer to the selected periods corresponding to the air masses originating from these regions. The average daily maximum concentrations of OH and HO_2* radicals for these periods are presented in Table 1. The average daily max OH concentrations were $6.89 \pm 1.10 \times 10^6$ cm^{-3} in PRD, $4.90 \pm 1.47 \times 10^6$ cm^{-3} in CEC, and $5.27 \pm 0.89 \times 10^6$ cm^{-3} in CNC, with a pronounced decrease from PRD to CEC (of 1.99×10^6 cm^{-3}). The average daily max HO_2* concentrations were $2.32 \pm 1.25 \times 10^8$ cm^{-3} in PRD, $2.36 \pm 0.92 \times 10^8$ cm^{-3} in CEC, and $1.82 \pm 1.02 \times 10^8$ cm^{-3} in CNC, with a slight increase of 0.04×10^8 cm^{-3} from

PRD to CEC and a more substantial decrease of 0.54 × 10^8 cm^{-3} from CEC to CNC. These trends suggest a declining atmospheric oxidation capacity from PRD to CNC.

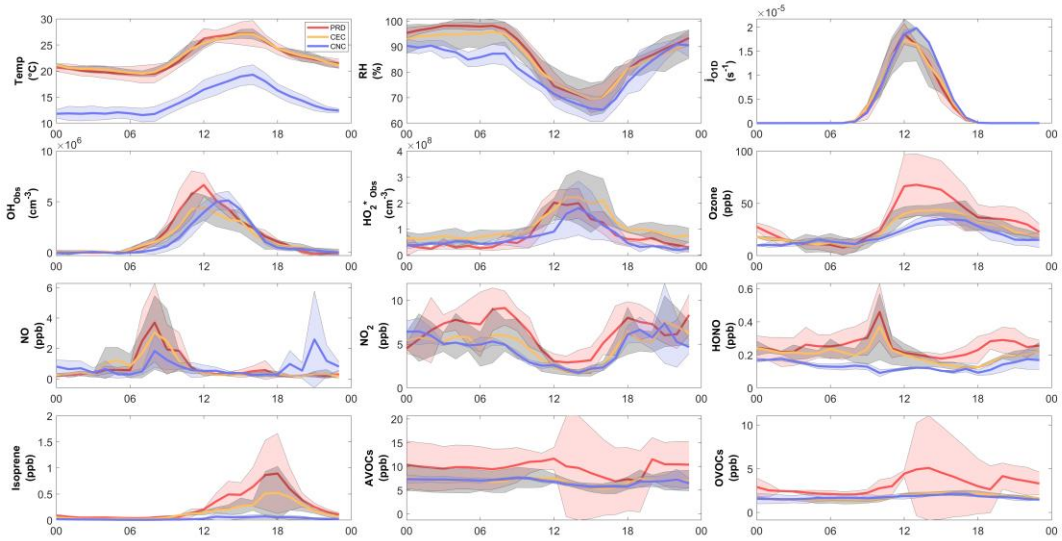

Figure 5 Average diurnal variations of (a) Temperature (b) Relative Humidity (c) J_{O1D} (d) OH (e)HO_2* (f) Ozone (g) NO (h) NO_2 (i)HONO (j)Isoprene (k) AVOCs (l) OVOCs. The solid-colored lines represent selected cases: orange for PRD, green for CEC, and blue for CNC. The light band represents the standard deviations of the mean. The increase in the standard deviations of VOCs and OVOCs during the PRD case is a result of absence of data on the afternoon of November 14th and large variations in on November 12th and 13th.

The precursor concentrations and meteorological parameters also varied across cases in terms of statistics (Tables 1 and S4) and diurnal variations (Figure 5). In the PRD case, the average concentrations are characteristic of a rural environment, with AVOCs at 9.70 ± 5.00 ppb, OVOCs at 3.20 ± 2.30 ppb, isoprene at 0.26 ± 0.34 ppb, NO_2 at 6.3 ± 2.5 ppb, and NO at 0.73 ± 1.09 ppb. The NO concentration was affected by traffic sources, as there were no other fresh emission source nearby, and the diurnal variation of NO showed a morning peak in all three cases (Figure 5). In the CEC case, a general reduction in anthropogenic influence is evident. AVOCs, OVOCs isoprene and NO_2 drop significantly to 6.90 ± 1.80 ppb, 1.70 ± 0.38 ppb, 0.16 ± 0.20 ppb, and 4.84 ± 2.23 ppb respectively. Meanwhile, NO levels remained close to PRD levels at 0.69 ± 1.00 ppb. In the CNC case, the air mass was more aged with reduced biogenic emissions, reflected in further decreases in isoprene and NO_2 to 0.03 ± 0.04 ppb and 4.52 ± 1.97 ppb, respectively, due to colder weather conditions. The temperature

decreased significantly from PRD to CNC, whereas the average peak photolysis frequency was comparable between PRD and CNC, as shown in Table 1.

3.2 Chemical budgets of OH and HO_2

To investigate the OH and HO_2 chemical budgets during the three distinct periods, we employed a box model constrained by observed concentrations of NO_X, VOCs, and relevant meteorological parameters in the selected cases (base scenario in which OH and HO_2 concentrations were not constrained by the measurements). The resulting OH and HO_2 budgets, displaying typical bell-shaped patterns, are illustrated in Figure 6. During midday (10:00–15:00), the primary source of HO_2 was the recycling of RO species, with rates of 3.22 ppb h^{-1} for PRD, 2.09 ppb h^{-1} for CEC, and 1.08 ppb h^{-1} for CNC. Additionally, HCHO photolysis contributed 0.75 ppb h^{-1}, 0.46 ppb h^{-1}, and 0.26 ppb h^{-1} for PRD, CEC, and CNC, respectively. The sinks of HO_2 varied among the cases with minor contribution from the uptake process, driven by radical termination mechanisms. The rate of radical self-reactions decreased from PRD to CNC. In contrast, NO_X-radical reactions between CEC and CNC were comparable, with respective rates of 0.39 ppb h^{-1} and 0.33 ppb h^{-1}, indicating a shift in radical termination mechanisms.

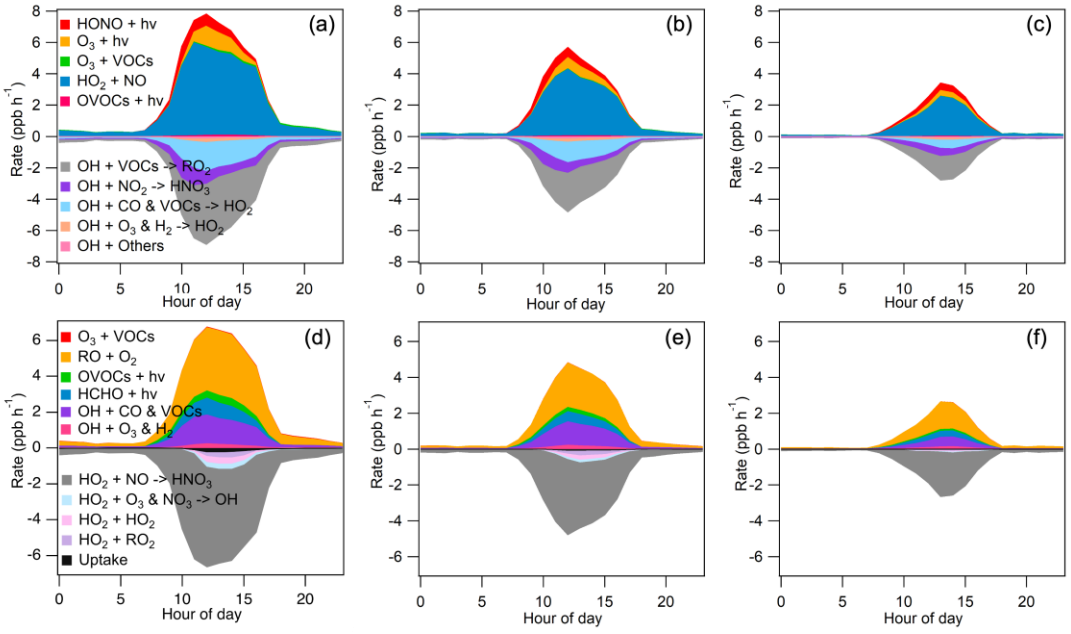

Figure 6 Chemical budgets of OH and HO_2 for PRD (a, d), CEC (b, e), and CNC (c, f) simulated using a chemical box model.

OH formation was predominantly driven by the HO_2 + NO reaction, contributing 5.18 ppb h^{-1}, 3.51 ppb h^{-1}, and 1.81 ppb h^{-1} (average for 10:00 – 15:00, referred to hereafter in this section) for PRD, CEC, and CNC, respectively. Additionally, contributions from ozone photolysis and HONO increased from PRD to CEC and then to CNC, with rates of 21.4%, 22.7%, and 24.6%, respectively. The primary sinks for OH included reactions with VOCs to produce RO_2, with rates of 3.31 ppb h^{-1}, 2.02 ppb h^{-1}, and 1.13 ppb h^{-1}, and reactions with CO and other VOCs to generate HO_2, contributing 1.55 ppb h^{-1}, 1.06 ppb h^{-1}, and 0.38 ppb h^{-1} for PRD, CEC, and CNC, respectively. These findings highlight the critical role of OH + VOC reactions in the chemical budget of OH.

3.3 Comparison of model with observation results

Modeled OH and HO_2 concentrations were evaluated by comparing them against observations. The observed HO_2^* serves as an upper limit for ambient HO_2 due to the interference from RO_2. The model calculated average daytime (08:00-16:00) RO_2 interference increased HO_2 by 127%, 117%, and 144% for PRD, CEC and CNC case, respectively. In the PRD case (Figure 7), which represents the most polluted and warmest environment among the three cases, the model slightly overestimated OH concentrations. However, the modeled HO_2 concentration was substantially higher than the observed HO_2^*, indicating an overprediction of HO_2. Similar overestimations have been reported at a rural site (Kanaya et al., 2012). For the CEC case (Figure 8), the modeled OH and HO_2 concentrations were moderately higher than the observed values during the daytime, consistent with findings from a rural forest site (Bottorff et al., 2023). In the CNC case (Figure 9), the model generally reproduced the observed OH trend, with HO_2 comparable to the observed HO_2^*. However, on December 7, it exhibited daytime overestimation of HO_X, similar to the PRD case. At night, both CNC and CEC showed lower modeled HO_2 concentrations compared to observed HO_2^*, which can be explained by the expected contribution of RO_2 interference to HO_2^* in the observations. To further investigate the possible reasons for the model-observation

discrepancies, sensitivity tests were conducted. The modeled RO_2 interference ratio was used to correct HO_2* values, roughly estimating ambient HO_2 as input for the tests.

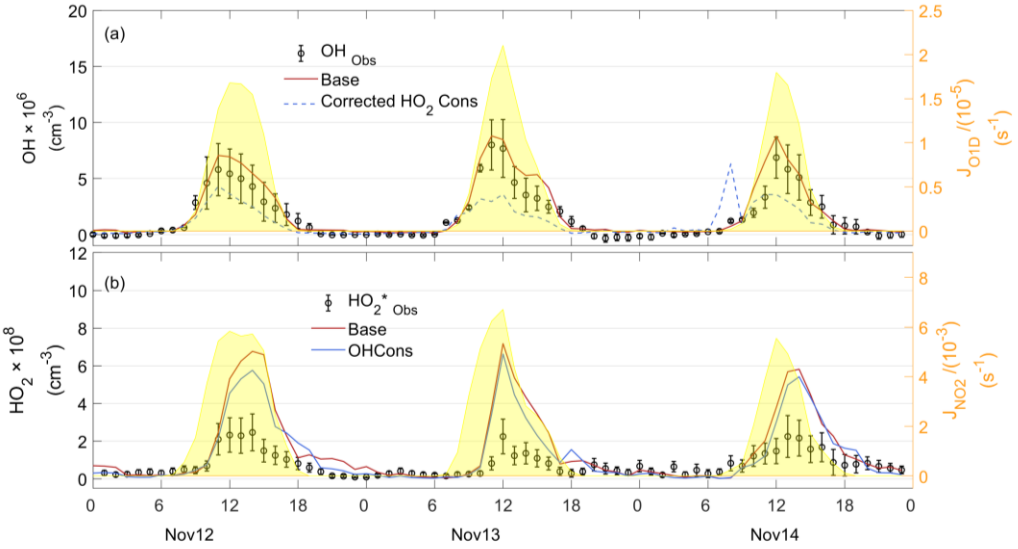

Figure 7 observed and simulated OH, observed HO_2*, and simulated HO_2 time series for the PRD case. The "Obs" subscript denotes the observation data. "Base" denotes the result of Baseline scenario as described in Box Model section. "Cons" denotes the results with additional constrained species compared to Base.

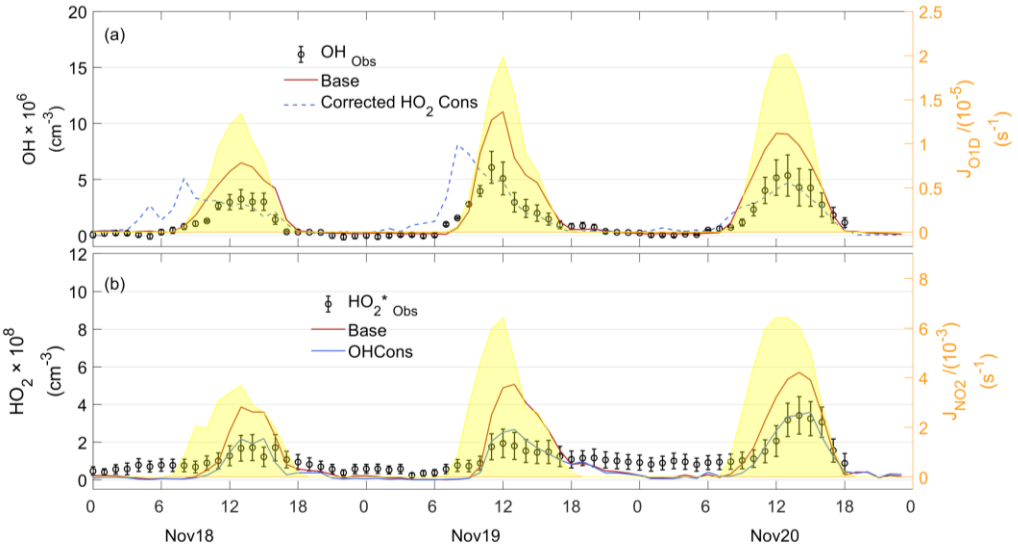

Figure 8 observed and simulated OH, observed HO_2*, and simulated HO_2 time series for the PRD case. The "Obs" subscript denotes the observation data. "Base" denotes the result of Baseline scenario as described in Box Model section. "Cons" denotes the results with additional constrained species compared to Base.

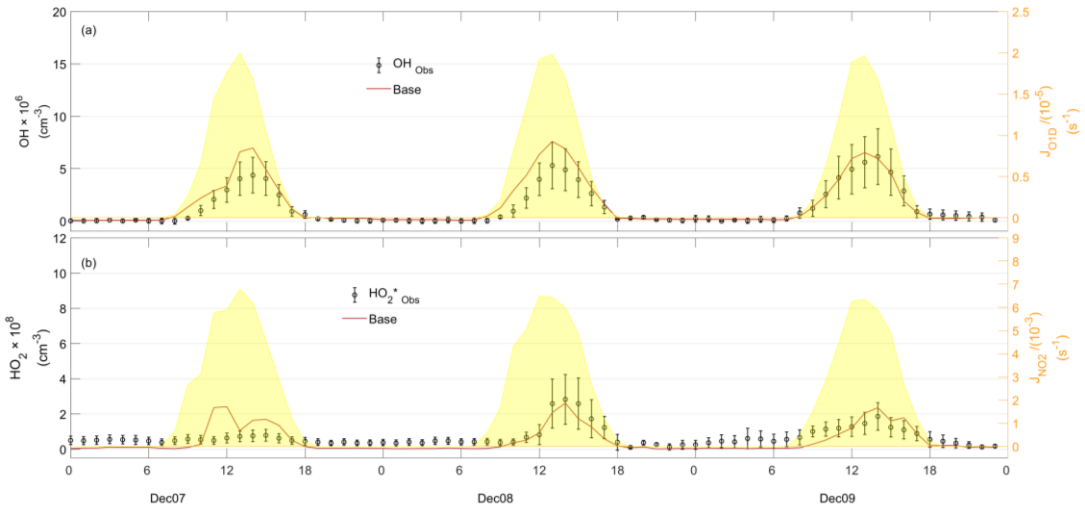

Figure 9 observed and simulated time series of OH and HO_2* for the CNC case. "Base" denotes the result of Baseline scenario as described in Box Model section.

3.3.1 Substantial overestimation of HO_2 in PRD case

To explain the HO_2 overprediction by the base model, we constrained OH or corrected HO_2* and compared these to the base case (without constraining OH and HO_2). Result shows that constraining corrected HO_2* causes the model to underestimate OH (blue line in Figure 7a), while constraining OH still leads substantially higher modeled HO_2 concentration than base model (blue line in Figure 7b). This result suggests that to align the modeled OH and HO_2 with observations, it may be necessary to introduce a strong, unknown process for HO_2 that efficiently recycles OH with a high yield (Kanaya et al., 2012).

3.3.2 Moderate overestimation of both OH and HO_2 radicals in CEC case

Unlike the PRD case, constraining either OH or corrected HO_2* in the CEC case generally reduces the daytime overestimation of both HO_2 and OH. These results indicate an additional sink for both OH and HO_2, as suggested by Bottorff et al. (2023). However, the OH concentration is overestimated in the morning when the corrected HO_2* was constrained, suggesting that there may be missing OH reactivity during this time. To further investigate the underlying causes, we examined the correlations between various pollutants. The significant negative correlation between CO and NO (R^2=0.49, p=0.01, Figure S6b) suggests that morning conditions in the CEC case may have been influenced by emission from fresh complete combustion during the CEC

case, while correlations in the PRD and CNC cases are not significant (Figures S6a and c). This indicates that the missing OH reactivity in the CEC case during the morning hours is possibly related to fresh vehicle emissions.

4. Implication for model overestimation of HO_X

OH and HO_2 are key species that determine the atmosphere's oxidative processes. Inaccurate modelling of their sinks can lead to significant overestimations of oxidation capacity, which may skew assessments of the impact of HO_X on air pollution and climate change. This problem is particularly pronounced in the case of ozone, a widespread photochemical pollutant. To demonstrate this issue, we compared results from two modelling scenarios: the first scenario was base case (as described in section 3.2), while the second scenario included constraints from all observational parameters, including measurements of OH and HO_2^*. Results for the scenario constrained by OH and corrected HO_2^* measurements are also showed in Figures 10 and 11.

As illustrated in Figure 10, not constraining free-radical measurement data in the chemical model (the orange lines) led to overestimates of ozone's photochemical production rates. Compared to scenarios constrained by OH and HO_2^*, in the PRD case, simulated midday O_X (O_3 + NO_2) formation rates in the base case were overestimated by 33% on average and 32% at peak O_X rates. In the CEC case, the overestimation was 79% on average and 89% at peak O_X rates, while in the CNC case, the smallest overestimation was 17% on average and 25% at peak. Since the ambient HO_2 concentration is lower than the constrained HO_2* concentration, the impact of the overestimated HO_x on ozone production rates might be even larger in such environments (the green lines in Figure 10).

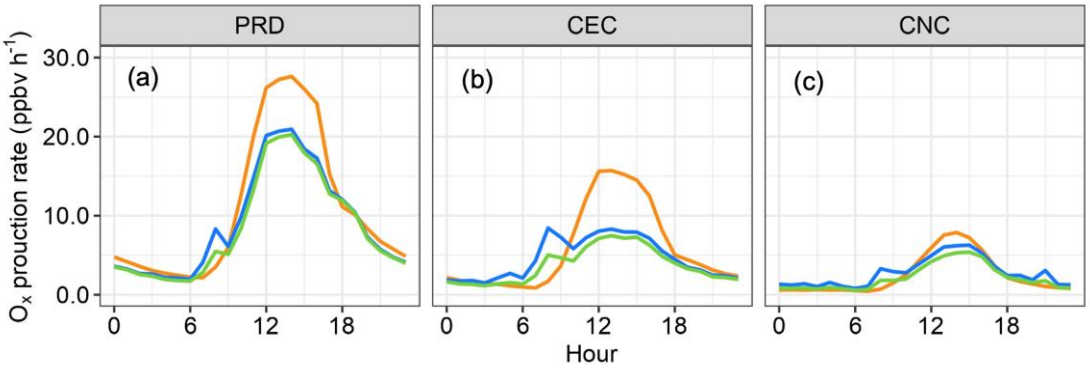

Figure 10 O_X (O_3+NO_2) photochemical production rates in three comparative cases: (a) PRD, (b) CEC, and (c) CNC. The orange, green, and blue lines represent rates modelled by excluding OH and HO_2^*, including OH with corrected HO_2^*, and including OH with uncorrected HO_2^*, respectively.

The overestimation of HO_X also significantly affected the simulated concentration of nitric acid (HNO_3), which is crucial for new particle formation and growth (Wang et al., 2020). Figure 11 illustrates that the chemical model moderately overestimated nitric acid production rates without the constraints of free-radical measurements (the orange lines). Compared to the scenarios constrained by OH and HO_2^*, the midday production rates of nitric acid were overestimated by 25%, 88%, and 31% in the PRD, CEC, and CNC cases, respectively. Such overestimations can considerably impact assessments of new particle formation and growth processes and their impact on air pollution and climate change. On the other hand, the impact on HNO_3 production is dominated by OH radical, therefore, measurement interference of HO_2 is negligible.

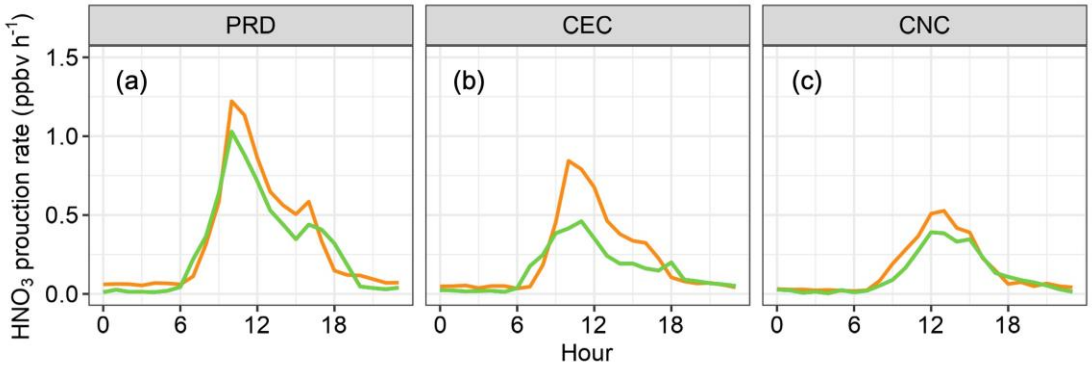

Figure 11 Modelled HNO_3 production rates in three comparative cases: (a) PRD, (b) CEC, and (c) CNC. The orange, green, and blue lines represent rates modelled by excluding OH and HO_2^*, including OH with corrected HO_2^*, and including OH with uncorrected HO_2^*, respectively. [The blue lines are covered by the green lines as the daytime HNO_3 production rate are determined by the constrained OH].

5. Conclusion

HO_2* and OH concentrations were measured using a chemical ionization mass spectrometer at a subtropical rural site in southern China from 12 November to 19 December 2022. The measurements indicated generally lower concentrations of OH and HO_2* than those observed in previous studies at various sites. The model estimated that interferences from RO_2 contributed to 44%-69% of the HO_2* throughout the

campaign. Backward trajectory analysis revealed three distinct phases characterised by sequentially decreasing pollution levels and temperatures. During the cold, clean period, model simulations closely matched the observed OH and HO_2* concentrations. However, during the warm, polluted period, the models overestimated HO_2 or both radicals. Model sensitivity analysis indicates that adding an OH cycling reaction from HO_2 or additional sinks of OH and HO_2 would largely reduce the model-observation discrepancy in different cases of this study. However, the exact chemical reactions remain to be identified. Our results are in line with previous studies indicating substantial gaps in our understanding of the sources and sinks of OH and HO_2 in certain environments. Our study provides additional evidence for the current incomplete understanding of the HO_X sources and sinks and calls for more research to resolve the model–observation mismatch found in this work and in previous studies.

The over-prediction of HO_X resulted in significant overestimation of the production rates of other secondary pollutants such as ozone and nitric acid at the site. It is critical to evaluate the capability of OH and HO_2 simulations in major chemical transport models and earth system models, as inaccurate simulations of OH and HO_2 may misguide the development of air pollution and global warming control strategies.

Data availability. All of the data used to produce this paper can be obtained by contacting Tao Wang (tao.wang@polyu.edu.hk).

Supplement. The online supplement for this article is available at:

Author contributions. TW conceived the HO_x research. TW, XW and YZ planned and organized the overall field campaign at Conghua. ZZ conducted the OH measurements using CIMS, with contributions from TW and WS, QC, and SH. XF, ZR, XL, AG, QW, CP, and XT performed the JNO_2 VOCs and OVOCs measurements. ZZ performed the chemical box modelling with contributions from TC and QC. TC, ZZ, and TW analysed the data and interpreted the result (ZZ analysed the time series and diurnal variations of observation data; TC interpreted the results of box model, investigated the missing sources; TW supervised and guided these processes). TC, ZZ, and TW wrote the paper. All of the authors reviewed and commented on the paper.

Competing interests. One author (Tao Wang) is a member of the editorial board of Atmospheric Chemistry and Physics. The authors have no other competing interests to declare.

Acknowledgments

We thank David Tanner, Dr. Wei Pu, Dr. Weihao Wang, and Dr. Zhe Wang for developing the PolyU-CIMS. We are also grateful to the Guangzhou Institute of Geochemistry, Chinese Academy of Sciences, for providing access to its station and data on trace gases.

Financial support.

This research was financially supported by the Hong Kong Research Grants Council (T24-504/17-N and 15223221 to Tao Wang), the National Science Foundation of China (42293322 to Tao Wang), and The Hong Kong Polytechnic University Postdoc Matching Fund Scheme (P0043403 to Tianshu Chen).

Reference

Berresheim, H., Elste, T., Tremmel, H. G., Allen, A. G., Hansson, H.-C., Rosman, K., Dal Maso, M., Mäkelä, J. M., Kulmala, M., and O'Dowd, C. D.: Gas-aerosol relationships of H_2SO_4, MSA, and OH: Observations in the coastal marine boundary layer at Mace Head, Ireland, Journal of Geophysical Research: Atmospheres, 107, PAR 5-1-PAR 5-12, https://doi.org/10.1029/2000JD000229, 2002.

Bottorff, B., Lew, M. M., Woo, Y., Rickly, P., Rollings, M. D., Deming, B., Anderson, D. C., Wood, E., Alwe, H. D., Millet, D. B., Weinheimer, A., Tyndall, G., Ortega, J., Dusanter, S., Leonardis, T., Flynn, J., Erickson, M., Alvarez, S., Rivera-Rios, J. C., Shutter, J. D., Keutsch, F., Helmig, D., Wang, W., Allen, H. M., Slade, J. H., Shepson, P. B., Bertman, S., and Stevens, P. S.: OH, HO_2, and RO_2 radical chemistry in a rural forest environment: measurements, model comparisons, and evidence of a missing radical sink, Atmospheric Chemistry and Physics, 23, 10287–10311, https://doi.org/10.5194/acp-23-10287-2023, 2023.

Carslaw, N., Creasey, D. J., Heard, D. E., Lewis, A. C., McQuaid, J. B., Pilling, M. J., Monks, P. S., Bandy, B. J., and Penkett, S. A.: Modeling OH, HO_2, and RO_2 radicals in the marine boundary layer: 1. Model construction and comparison with field measurements, J. Geophys. Res., 104, 30241–30255, https://doi.org/10.1029/1999JD900783, 1999.

Chen, Q., Xia, M., Peng, X., Yu, C., Sun, P., Li, Y., Liu, Y., Xu, Z., Xu, Z., Wu, R., Nie, W., Ding, A., Zhao, Y., and Wang, T.: Large Daytime Molecular Chlorine Missing Source at a Suburban Site

in East China, JGR Atmospheres, 127, https://doi.org/10.1029/2021JD035796, 2022.

Edwards, G. D., Cantrell, C. A., Stephens, S., Hill, B., Goyea, O., Shetter, R. E., Mauldin, R. L., Kosciuch, E., Tanner, D. J., and Eisele, F. L.: Chemical Ionization Mass Spectrometer Instrument for the Measurement of Tropospheric HO_2 and RO_2, Anal. Chem., 75, 5317–5327, https://doi.org/10.1021/ac034402b, 2003.

Eisele, F. L. and Tanner, D. J.: Ion-assisted tropospheric OH measurements, J. Geophys. Res., 96, 9295, https://doi.org/10.1029/91JD00198, 1991.

Eisele, F. L. and Tanner, D. J.: Measurement of the gas phase concentration of H_2SO_4 and methane sulfonic acid and estimates of H_2SO_4 production and loss in the atmosphere, Journal of Geophysical Research: Atmospheres, 98, 9001–9010, https://doi.org/10.1029/93JD00031, 1993.

Feiner, P. A., Brune, W. H., Miller, D. O., Zhang, L., Cohen, R. C., Romer, P. S., Goldstein, A. H., Keutsch, F. N., Skog, K. M., Wennberg, P. O., Nguyen, T. B., Teng, A. P., DeGouw, J., Koss, A., Wild, R. J., Brown, S. S., Guenther, A., Edgerton, E., Baumann, K., and Fry, J. L.: Testing Atmospheric Oxidation in an Alabama Forest, Journal of the Atmospheric Sciences, 73, 4699–4710, https://doi.org/10.1175/JAS-D-16-0044.1, 2016.

Fuchs, H., Bohn, B., Hofzumahaus, A., Holland, F., Lu, K. D., Nehr, S., Rohrer, F., and Wahner, A.: Detection of HO_2 by laser-induced fluorescence: calibration and interferences from RO_2 radicals, Atmospheric Measurement Techniques, 4, 1209–1225, https://doi.org/10.5194/amt-4-1209-2011, 2011.

Fuchs, H., Acir, I.-H., Bohn, B., Brauers, T., Dorn, H.-P., Häseler, R., Hofzumahaus, A., Holland, F., Kaminski, M., Li, X., Lu, K., Lutz, A., Nehr, S., Rohrer, F., Tillmann, R., Wegener, R., and Wahner, A.: OH regeneration from methacrolein oxidation investigated in the atmosphere simulation chamber SAPHIR, Atmos. Chem. Phys., 14, 7895–7908, https://doi.org/10.5194/acp-14-7895-2014, 2014.

Griffith, S. M., Hansen, R. F., Dusanter, S., Stevens, P. S., Alaghmand, M., Bertman, S. B., Carroll, M. A., Erickson, M., Galloway, M., Grossberg, N., Hottle, J., Hou, J., Jobson, B. T., Kammrath, A., Keutsch, F. N., Lefer, B. L., Mielke, L. H., O'Brien, A., Shepson, P. B., Thurlow, M., Wallace, W., Zhang, N., and Zhou, X. L.: OH and HO_2 radical chemistry during PROPHET 2008 and CABINEX 2009 - Part 1: Measurements and model comparison, Atmospheric Chemistry and Physics, 13, 5403–5423, https://doi.org/10.5194/acp-13-5403-2013, 2013.

Guo, J., Wang, Z., Tao Wang, and Zhang, X.: Theoretical evaluation of different factors affecting the HO_2 uptake coefficient driven by aqueous-phase first-order loss reaction, Science of The Total Environment, 683, 146–153, https://doi.org/10.1016/j.scitotenv.2019.05.237, 2019.

Hanke, M., Uecker, J., Reiner, T., and Arnold, F.: Atmospheric peroxy radicals: ROXMAS, a new mass-spectrometric methodology for speciated measurements of HO_2 and $\sum RO_2$ and first

results, International Journal of Mass Spectrometry, 213, 91–99, https://doi.org/10.1016/S1387-3806(01)00548-6, 2002.

Hansen, R. F., Griffith, S. M., Dusanter, S., Rickly, P. S., Stevens, P. S., Bertman, S. B., Carroll, M. A., Erickson, M. H., Flynn, J. H., Grossberg, N., Jobson, B. T., Lefer, B. L., and Wallace, H. W.: Measurements of total hydroxyl radical reactivity during CABINEX 2009 – Part 1: field measurements, Atmos. Chem. Phys., 14, 2923–2937, https://doi.org/10.5194/acp-14-2923-2014, 2014.

Heard, D. E. and Pilling, M. J.: Measurement of OH and HO_2 in the Troposphere, Chem. Rev., 103, 5163–5198, https://doi.org/10.1021/cr020522s, 2003.

Hens, K., Novelli, A., Martinez, M., Auld, J., Axinte, R., Bohn, B., Fischer, H., Keronen, P., Kubistin, D., Nölscher, A. C., Oswald, R., Paasonen, P., Petäjä, T., Regelin, E., Sander, R., Sinha, V., Sipilä, M., Taraborrelli, D., Tatum Ernest, C., Williams, J., Lelieveld, J., and Harder, H.: Observation and modelling of HO_x radicals in a boreal forest, Atmospheric Chemistry and Physics, 14, 8723–8747, https://doi.org/10.5194/acp-14-8723-2014, 2014.

Hofzumahaus, A., Rohrer, F., Lu, K., Bohn, B., Brauers, T., Chang, C.-C., Fuchs, H., Holland, F., Kita, K., Kondo, Y., Li, X., Lou, S., Shao, M., Zeng, L., Wahner, A., and Zhang, Y.: Amplified Trace Gas Removal in the Troposphere, Science, 324, 1702–1704, https://doi.org/10.1126/science.1164566, 2009.

Jacob, D.: Heterogeneous chemistry and tropospheric ozone, Atmospheric Environment, 34, 2131–2159, https://doi.org/10.1016/S1352-2310(99)00462-8, 2000.

Jeong, D., Seco, R., Emmons, L., Schwantes, R., Liu, Y., McKinney, K. A., Martin, S. T., Keutsch, F. N., Gu, D., Guenther, A. B., Vega, O., Tota, J., Souza, R. A. F., Springston, S. R., Watson, T. B., and Kim, S.: Reconciling Observed and Predicted Tropical Rainforest OH Concentrations, JGR Atmospheres, 127, https://doi.org/10.1029/2020JD032901, 2022.

Kanaya, Y., Cao, R., Kato, S., Miyakawa, Y., Kajii, Y., Tanimoto, H., Yokouchi, Y., Mochida, M., Kawamura, K., and Akimoto, H.: Chemistry of OH and HO_2 radicals observed at Rishiri Island, Japan, in September 2003: Missing daytime sink of HO_2 and positive nighttime correlations with monoterpenes, J. Geophys. Res., 112, D11308, https://doi.org/10.1029/2006JD007987, 2007.

Kanaya, Y., Hofzumahaus, A., Dorn, H.-P., Brauers, T., Fuchs, H., Holland, F., Rohrer, F., Bohn, B., Tillmann, R., Wegener, R., Wahner, A., Kajii, Y., Miyamoto, K., Nishida, S., Watanabe, K., Yoshino, A., Kubistin, D., Martinez, M., Rudolf, M., Harder, H., Berresheim, H., Elste, T., Plass-Dülmer, C., Stange, G., Kleffmann, J., Elshorbany, Y., and Schurath, U.: Comparisons of observed and modeled OH and HO_2 concentrations during the ambient measurement period of the HO_xComp field campaign, Atmospheric Chemistry and Physics, 12, 2567–2585, https://doi.org/10.5194/acp-12-2567-2012, 2012.

Kim, S., Wolfe, G. M., Mauldin, L., Cantrell, C., Guenther, A., Karl, T., Turnipseed, A., Greenberg,

J., Hall, S. R., Ullmann, K., Apel, E., Hornbrook, R., Kajii, Y., Nakashima, Y., Keutsch, F. N., DiGangi, J. P., Henry, S. B., Kaser, L., Schnitzhofer, R., Graus, M., Hansel, A., Zheng, W., and Flocke, F. F.: Evaluation of HO_x sources and cycling using measurement-constrained model calculations in a 2-methyl-3-butene-2-ol (MBO) and monoterpene (MT) dominated ecosystem, Atmospheric Chemistry and Physics, 13, 2031–2044, https://doi.org/10.5194/acp-13-2031-2013, 2013.

Kürten, A., Rondo, L., Ehrhart, S., and Curtius, J.: Calibration of a Chemical Ionization Mass Spectrometer for the Measurement of Gaseous Sulfuric Acid, J. Phys. Chem. A, 116, 6375–6386, https://doi.org/10.1021/jp212123n, 2012.

Lelieveld, J., Butler, T. M., Crowley, J. N., Dillon, T. J., Fischer, H., Ganzeveld, L., Harder, H., Lawrence, M. G., Martinez, M., Taraborrelli, D., and Williams, J.: Atmospheric oxidation capacity sustained by a tropical forest, Nature, 452, 737–740, https://doi.org/10.1038/nature06870, 2008.

Lew, M. M., Rickly, P. S., Bottorff, B. P., Reidy, E., Sklaveniti, S., Léonardis, T., Locoge, N., Dusanter, S., Kundu, S., Wood, E., and Stevens, P. S.: OH and HO_2 radical chemistry in a midlatitude forest: measurements and model comparisons, Atmospheric Chemistry and Physics, 20, 9209–9230, https://doi.org/10.5194/acp-20-9209-2020, 2020.

Lou, S., Holland, F., Rohrer, F., Lu, K., Bohn, B., Brauers, T., Chang, C. C., Fuchs, H., Häseler, R., Kita, K., Kondo, Y., Li, X., Shao, M., Zeng, L., Wahner, A., Zhang, Y., Wang, W., and Hofzumahaus, A.: Atmospheric OH reactivities in the Pearl River Delta – China in summer 2006: measurement and model results, Atmos. Chem. Phys., 10, 11243–11260, https://doi.org/10.5194/acp-10-11243-2010, 2010.

Ma, X., Tan, Z., Lu, K., Yang, X., Liu, Y., Li, S., Li, X., Chen, S., Novelli, A., Cho, C., Zeng, L., Wahner, A., and Zhang, Y.: Winter photochemistry in Beijing: Observation and model simulation of OH and HO2 radicals at an urban site, Science of The Total Environment, 685, 85–95, https://doi.org/10.1016/j.scitotenv.2019.05.329, 2019.

Ma, X., Tan, Z., Lu, K., Yang, X., Chen, X., Wang, H., Chen, S., Fang, X., Li, S., Li, X., Liu, J., Liu, Y., Lou, S., Qiu, W., Wang, H., Zeng, L., and Zhang, Y.: OH and HO_2 radical chemistry at a suburban site during the EXPLORE-YRD campaign in 2018, Atmospheric Chemistry and Physics, 22, 7005–7028, https://doi.org/10.5194/acp-22-7005-2022, 2022.

Mallik, C., Tomsche, L., Bourtsoukidis, E., Crowley, J. N., Derstroff, B., Fischer, H., Hafermann, S., Hüser, I., Javed, U., Keßel, S., Lelieveld, J., Martinez, M., Meusel, H., Novelli, A., Phillips, G. J., Pozzer, A., Reiffs, A., Sander, R., Taraborrelli, D., Sauvage, C., Schuladen, J., Su, H., Williams, J., and Harder, H.: Oxidation processes in the eastern Mediterranean atmosphere: evidence from the modelling of HO_x measurements over Cyprus, Atmospheric Chemistry and Physics, 18, 10825–10847, https://doi.org/10.5194/acp-18-10825-2018, 2018.

Mao, J., Ren, X., Zhang, L., Van Duin, D. M., Cohen, R. C., Park, J.-H., Goldstein, A. H., Paulot, F., Beaver, M. R., Crounse, J. D., Wennberg, P. O., DiGangi, J. P., Henry, S. B., Keutsch, F. N.,

Park, C., Schade, G. W., Wolfe, G. M., Thornton, J. A., and Brune, W. H.: Insights into hydroxyl measurements and atmospheric oxidation in a California forest, Atmos. Chem. Phys., 12, 8009–8020, https://doi.org/10.5194/acp-12-8009-2012, 2012.

Mauldin III, R. L., Kosciuch, E., Henry, B., Eisele, F. L., Shetter, R., Lefer, B., Chen, G., Davis, D., Huey, G., and Tanner, D.: Measurements of OH, HO_2+RO_2, H_2SO_4, and MSA at the South Pole during ISCAT 2000, Atmospheric Environment, 38, 5423–5437, https://doi.org/10.1016/j.atmosenv.2004.06.031, 2004.

Muller, J. B. A., Elste, T., Plass-Dülmer, C., Stange, G., Holla, R., Claude, A., Englert, J., Gilge, S., and Kubistin, D.: A novel semi-direct method to measure OH reactivity by chemical ionization mass spectrometry (CIMS), Atmos. Meas. Tech., 11, 4413–4433, https://doi.org/10.5194/amt-11-4413-2018, 2018.

Novelli, A., Hens, K., Tatum Ernest, C., Kubistin, D., Regelin, E., Elste, T., Plass-Dülmer, C., Martinez, M., Lelieveld, J., and Harder, H.: Characterisation of an inlet pre-injector laser-induced fluorescence instrument for the measurement of atmospheric hydroxyl radicals, Atmos. Meas. Tech., 7, 3413–3430, https://doi.org/10.5194/amt-7-3413-2014, 2014.

Novelli, A., Vereecken, L., Bohn, B., Dorn, H.-P., Gkatzelis, G. I., Hofzumahaus, A., Holland, F., Reimer, D., Rohrer, F., Rosanka, S., Taraborrelli, D., Tillmann, R., Wegener, R., Yu, Z., Kiendler-Scharr, A., Wahner, A., and Fuchs, H.: Importance of isomerization reactions for OH radical regeneration from the photo-oxidation of isoprene investigated in the atmospheric simulation chamber SAPHIR, Atmos. Chem. Phys., 20, 3333–3355, https://doi.org/10.5194/acp-20-3333-2020, 2020.

Sjostedt, S. J., Huey, L. G., Tanner, D. J., Peischl, J., Chen, G., Dibb, J. E., Lefer, B., Hutterli, M. A., Beyersdorf, A. J., Blake, N. J., Blake, D. R., Sueper, D., Ryerson, T., Burkhart, J., and Stohl, A.: Observations of hydroxyl and the sum of peroxy radicals at Summit, Greenland during summer 2003, Atmospheric Environment, 41, 5122–5137, https://doi.org/10.1016/j.atmosenv.2006.06.065, 2007.

Slater, E. J., Whalley, L. K., Woodward-Massey, R., Ye, C., Lee, J. D., Squires, F., Hopkins, J. R., Dunmore, R. E., Shaw, M., Hamilton, J. F., Lewis, A. C., Crilley, L. R., Kramer, L., Bloss, W., Vu, T., Sun, Y., Xu, W., Yue, S., Ren, L., Acton, W. J. F., Hewitt, C. N., Wang, X., Fu, P., and Heard, D. E.: Elevated levels of OH observed in haze events during wintertime in central Beijing, Atmospheric Chemistry and Physics, 20, 14847–14871, https://doi.org/10.5194/acp-20-14847-2020, 2020.

Stone, D., Whalley, L. K., and Heard, D. E.: Tropospheric OH and HO_2 radicals: field measurements and model comparisons, Chem. Soc. Rev., 41, 6348, https://doi.org/10.1039/c2cs35140d, 2012.

Tan, D., Faloona, I., Simpas, J. B., Brune, W., Shepson, P. B., Couch, T. L., Sumner, A. L., Carroll, M. A., Thornberry, T., Apel, E., Riemer, D., and Stockwell, W.: HO_x budgets in a deciduous forest: Results from the PROPHET summer 1998 campaign, J. Geophys. Res., 106, 24407–24427,

https://doi.org/10.1029/2001JD900016, 2001.

Tan, Z., Fuchs, H., Lu, K., Hofzumahaus, A., Bohn, B., Broch, S., Dong, H., Gomm, S., Häseler, R., He, L., Holland, F., Li, X., Liu, Y., Lu, S., Rohrer, F., Shao, M., Wang, B., Wang, M., Wu, Y., Zeng, L., Zhang, Y., Wahner, A., and Zhang, Y.: Radical chemistry at a rural site (Wangdu) in the North China Plain: observation and model calculations of OH, HO_2 and RO_2 radicals, Atmospheric Chemistry and Physics, 17, 663–690, https://doi.org/10.5194/acp-17-663-2017, 2017.

Tan, Z., Rohrer, F., Lu, K., Ma, X., Bohn, B., Broch, S., Dong, H., Fuchs, H., Gkatzelis, G. I., Hofzumahaus, A., Holland, F., Li, X., Liu, Y., Liu, Y., Novelli, A., Shao, M., Wang, H., Wu, Y., Zeng, L., Hu, M., Kiendler-Scharr, A., Wahner, A., and Zhang, Y.: Wintertime photochemistry in Beijing: observations of RO_x radical concentrations in the North China Plain during the BEST-ONE campaign, Atmospheric Chemistry and Physics, 18, 12391–12411, https://doi.org/10.5194/acp-18-12391-2018, 2018.

Tan, Z., Lu, K., Hofzumahaus, A., Fuchs, H., Bohn, B., Holland, F., Liu, Y., Rohrer, F., Shao, M., Sun, K., Wu, Y., Zeng, L., Zhang, Y., Zou, Q., Kiendler-Scharr, A., Wahner, A., and Zhang, Y.: Experimental budgets of OH, HO_2, and RO_2 radicals and implications for ozone formation in the Pearl River Delta in China 2014, Atmospheric Chemistry and Physics, 19, 7129–7150, https://doi.org/10.5194/acp-19-7129-2019, 2019.

Tanner, D. J. and Eisele, F. L.: Present OH measurement limits and associated uncertainties, J. Geophys. Res., 100, 2883, https://doi.org/10.1029/94JD02609, 1995.

Tanner, D. J., Jefferson, A., and Eisele, F. L.: Selected ion chemical ionization mass spectrometric measurement of OH, J. Geophys. Res., 102, 6415–6425, https://doi.org/10.1029/96JD03919, 1997.

Thames, A. B., Brune, W. H., Miller, D. O., Allen, H. M., Apel, E. C., Blake, D. R., Bui, T. P., Commane, R., Crounse, J. D., Daube, B. C., Diskin, G. S., DiGangi, J. P., Elkins, J. W., Hall, S. R., Hanisco, T. F., Hannun, R. A., Hintsa, E., Hornbrook, R. S., Kim, M. J., McKain, K., Moore, F. L., Nicely, J. M., Peischl, J., Ryerson, T. B., St. Clair, J. M., Sweeney, C., Teng, A., Thompson, C. R., Ullmann, K., Wennberg, P. O., and Wolfe, G. M.: Missing OH reactivity in the global marine boundary layer, Atmospheric Chemistry and Physics, 20, 4013–4029, https://doi.org/10.5194/acp-20-4013-2020, 2020.

Wang, M., Kong, W., Marten, R., He, X.-C., Chen, D., Pfeifer, J., Heitto, A., Kontkanen, J., Dada, L., Kürten, A., Yli-Juuti, T., Manninen, H. E., Amanatidis, S., Amorim, A., Baalbaki, R., Baccarini, A., Bell, D. M., Bertozzi, B., Bräkling, S., Brilke, S., Murillo, L. C., Chiu, R., Chu, B., De Menezes, L.-P., Duplissy, J., Finkenzeller, H., Carracedo, L. G., Granzin, M., Guida, R., Hansel, A., Hofbauer, V., Krechmer, J., Lehtipalo, K., Lamkaddam, H., Lampimäki, M., Lee, C. P., Makhmutov, V., Marie, G., Mathot, S., Mauldin, R. L., Mentler, B., Müller, T., Onnela, A., Partoll, E., Petäjä, T., Philippov, M., Pospisilova, V., Ranjithkumar, A., Rissanen, M., Rörup, B., Scholz, W., Shen, J., Simon, M., Sipilä, M., Steiner, G., Stolzenburg, D., Tham, Y. J., Tomé, A., Wagner, A. C., Wang, D. S., Wang, Y., Weber, S. K., Winkler, P. M., Wlasits, P. J., Wu, Y., Xiao, M., Ye, Q., Zauner-Wieczorek, M.,

Zhou, X., Volkamer, R., Riipinen, I., Dommen, J., Curtius, J., Baltensperger, U., Kulmala, M., Worsnop, D. R., Kirkby, J., Seinfeld, J. H., El-Haddad, I., Flagan, R. C., and Donahue, N. M.: Rapid growth of new atmospheric particles by nitric acid and ammonia condensation, Nature, 581, 184–189, https://doi.org/10.1038/s41586-020-2270-4, 2020.

Wang, X., Jacob, D. J., Eastham, S. D., Sulprizio, M. P., Zhu, L., Chen, Q., Alexander, B., Sherwen, T., Evans, M. J., Lee, B. H., Haskins, J. D., Lopez-Hilfiker, F. D., Thornton, J. A., Huey, G. L., and Liao, H.: The role of chlorine in global tropospheric chemistry, Atmospheric Chemistry and Physics, 19, 3981–4003, https://doi.org/10.5194/acp-19-3981-2019, 2019.

Wennberg, P. O., Bates, K. H., Crounse, J. D., Dodson, L. G., McVay, R. C., Mertens, L. A., Nguyen, T. B., Praske, E., Schwantes, R. H., Smarte, M. D., St Clair, J. M., Teng, A. P., Zhang, X., and Seinfeld, J. H.: Gas-Phase Reactions of Isoprene and Its Major Oxidation Products, Chem. Rev., 118, 3337–3390, https://doi.org/10.1021/acs.chemrev.7b00439, 2018.

Whalley, L. K., Edwards, P. M., Furneaux, K. L., Goddard, A., Ingham, T., Evans, M. J., Stone, D., Hopkins, J. R., Jones, C. E., Karunaharan, A., Lee, J. D., Lewis, A. C., Monks, P. S., Moller, S. J., and Heard, D. E.: Quantifying the magnitude of a missing hydroxyl radical source in a tropical rainforest, Atmos. Chem. Phys., 11, 7223–7233, https://doi.org/10.5194/acp-11-7223-2011, 2011.

Whalley, L. K., Blitz, M. A., Desservettaz, M., Seakins, P. W., and Heard, D. E.: Reporting the sensitivity of laser-induced fluorescence instruments used for HO_2 detection to an interference from RO_2 radicals and introducing a novel approach that enables HO_2 and certain RO_2 types to be selectively measured, Atmospheric Measurement Techniques, 6, 3425–3440, https://doi.org/10.5194/amt-6-3425-2013, 2013.

Wolfe, G. M., Marvin, M. R., Roberts, S. J., Travis, K. R., and Liao, J.: The Framework for 0-D Atmospheric Modeling (F0AM) v3.1, Geosci. Model Dev., 9, 3309–3319, https://doi.org/10.5194/gmd-9-3309-2016, 2016.

Woodward-Massey, R., Slater, E. J., Alen, J., Ingham, T., Cryer, D. R., Stimpson, L. M., Ye, C., Seakins, P. W., Whalley, L. K., and Heard, D. E.: Implementation of a chemical background method for atmospheric OH measurements by laser-induced fluorescence: characterisation and observations from the UK and China, Atmospheric Measurement Techniques, 13, 3119–3146, https://doi.org/10.5194/amt-13-3119-2020, 2020.

Xu, Z., Xue, L., Wang, T., Xia, T., Gao, Y., Louie, P. K. K., and Luk, C. W. Y.: Measurements of Peroxyacetyl Nitrate at a Background Site in the Pearl River Delta Region: Production Efficiency and Regional Transport, Aerosol Air Qual. Res., 15, 833–841, https://doi.org/10.4209/aaqr.2014.11.0275, 2015.

Yang, X., Lu, K., Ma, X., Liu, Y., Wang, H., Hu, R., Li, X., Lou, S., Chen, S., Dong, H., Wang, F., Wang, Y., Zhang, G., Li, S., Yang, S., Yang, Y., Kuang, C., Tan, Z., Chen, X., Qiu, P., Zeng, L., Xie, P., and Zhang, Y.: Observations and modeling of OH and HO2 radicals in Chengdu, China in summer 2019, Science of The Total Environment, 772, 144829,

https://doi.org/10.1016/j.scitotenv.2020.144829, 2021.

Yang, X., Lu, K., Ma, X., Gao, Y., Tan, Z., Wang, H., Chen, X., Li, X., Huang, X., He, L., Tang, M., Zhu, B., Chen, S., Dong, H., Zeng, L., and Zhang, Y.: Radical chemistry in the Pearl River Delta: observations and modeling of OH and HO_2 radicals in Shenzhen in 2018, Atmospheric Chemistry and Physics, 22, 12525–12542, https://doi.org/10.5194/acp-22-12525-2022, 2022.

Yang, Y., Shao, M., Wang, X., Nölscher, A. C., Kessel, S., Guenther, A., and Williams, J.: Towards a quantitative understanding of total OH reactivity: A review, Atmospheric Environment, 134, 147–161, https://doi.org/10.1016/j.atmosenv.2016.03.010, 2016.

Zou, Z., Chen, Q., Xia, M., Yuan, Q., Chen, Y., Wang, Y., Xiong, E., Wang, Z., and Wang, T.: OH measurements in the coastal atmosphere of South China: possible missing OH sinks in aged air masses, Atmospheric Chemistry and Physics, 23, 7057–7074, https://doi.org/10.5194/acp-23-7057-2023, 2023.

Supporting Information for

Observation and modelling of OH and HO_2* radicals at a subtropical rural site and implications for secondary pollutants

Zhouxing Zou[1#], Tianshu Chen[1#], Qianjie Chen[1], Weihang Sun[1], Shichun Han[1], Zhuoyue Ren[2], Xinyi Li[2], Wei Song[2], Aoqi Ge[2], Qi Wang[2], Xiao Tian[2], Chenglei Pei[3], Xinming Wang[2], Yanli Zhang[2], and Tao Wang[1]

[#] These authors contributed equally to this work

[1] Department of Civil and Environmental Engineering, The Hong Kong Polytechnic University, Hong Kong, China

[2] Guangzhou Institute of Geochemistry, Chinese Academy of Sciences, Guangzhou, China

[3]Guangdong Province Guangzhou Ecological Environment Monitoring Center Station, Guangzhou 510030, China.

Correspondence to: Tao Wang (tao.wang@polyu.edu.hk)

Contents of this File

20 pages

Figures: S1 to S10

Tables: S1 to S5

Text: S1 to S6

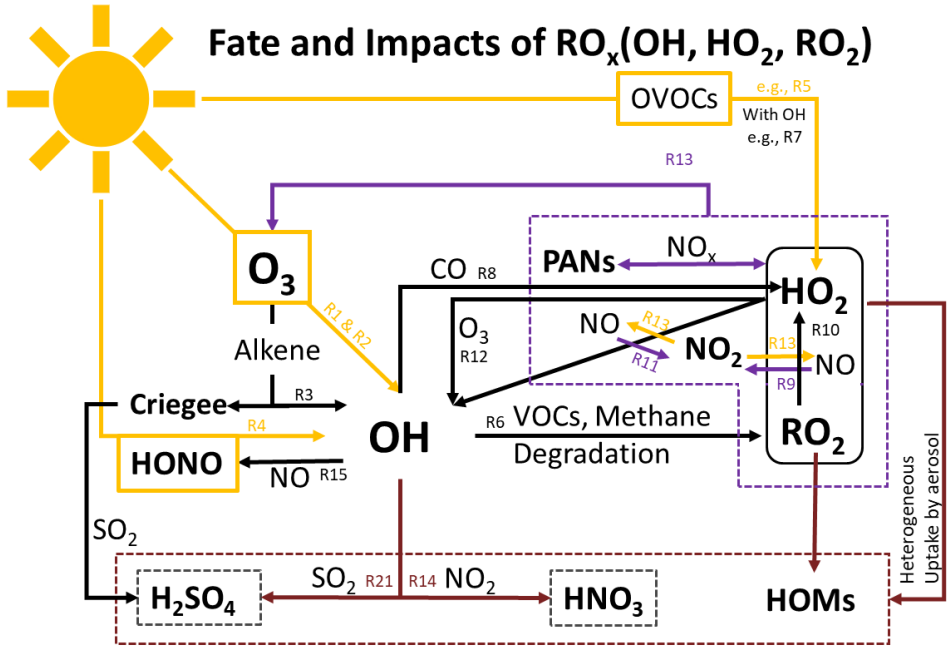

Figure S1 Schematic of the RO_x family's photochemical pathway. Photolysis reactions are highlighted in yellow, reactions contributing to secondary aerosol production are marked in brown; and reactions associated with photochemical pollution are indicated in purple. The chemical reactions (R1 to R21) referenced in Table S1.

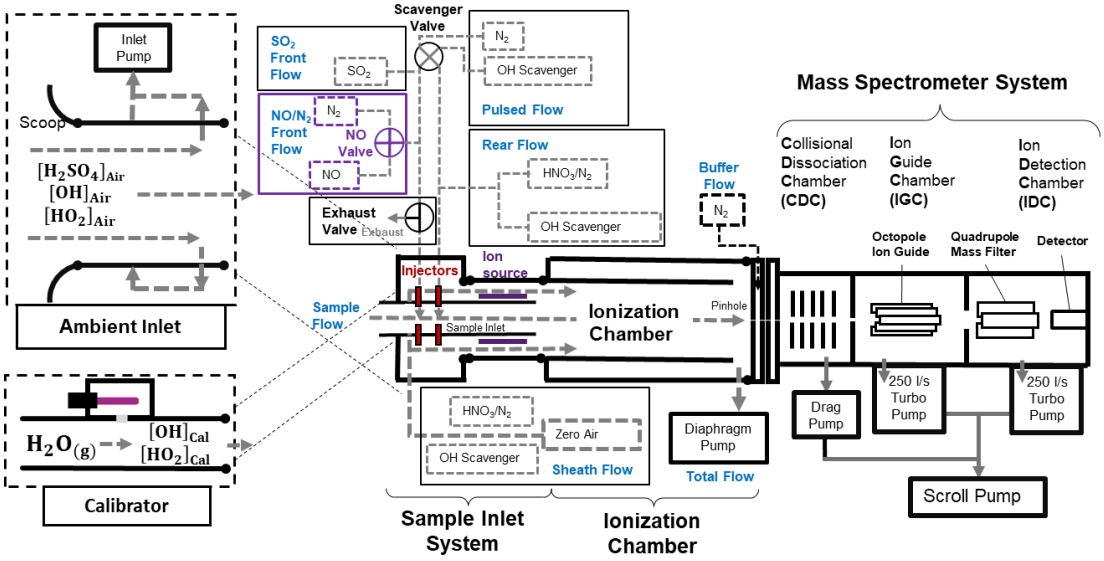

Figure S2 Schematic diagram of the PolyU-CIMS system. The CIMS is composed of two detachable components: the ambient inlet and the calibrator; and the main body, which includes the sample inlet system, ionization chamber, and the mass spectrometer system. The frames labeled in purple highlight the additional valve

incorporated for HO_2 measurement. Further details on setup, measurement principles of the CIMS are available in a previous study (Zou et al., 2023) and Text S1.

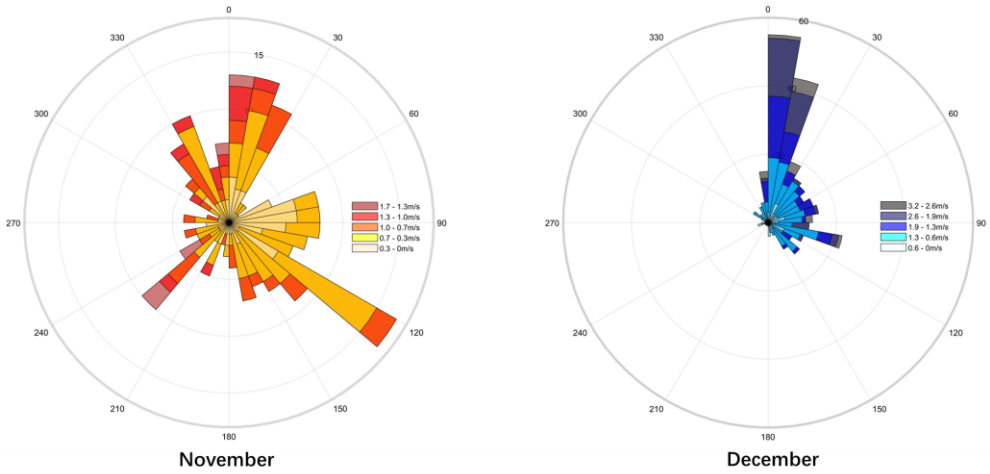

Figure S3 The wind rose for November and December.

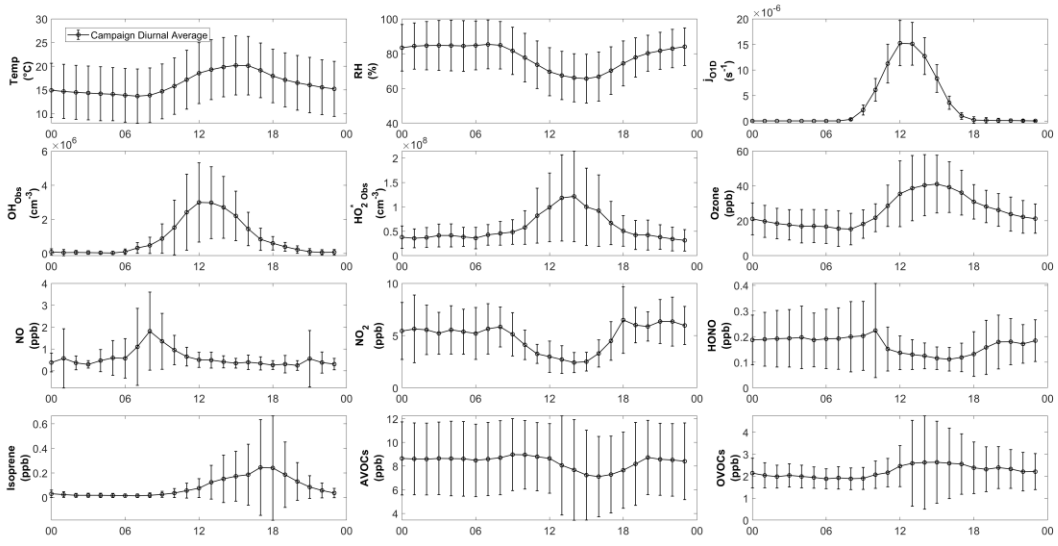

Figure S4 Diurnal profiles of average concentration of HO_2*, OH, meteorological data and trace gases of the whole campaign. The shaded error bars represent standard deviations of the averaged data.

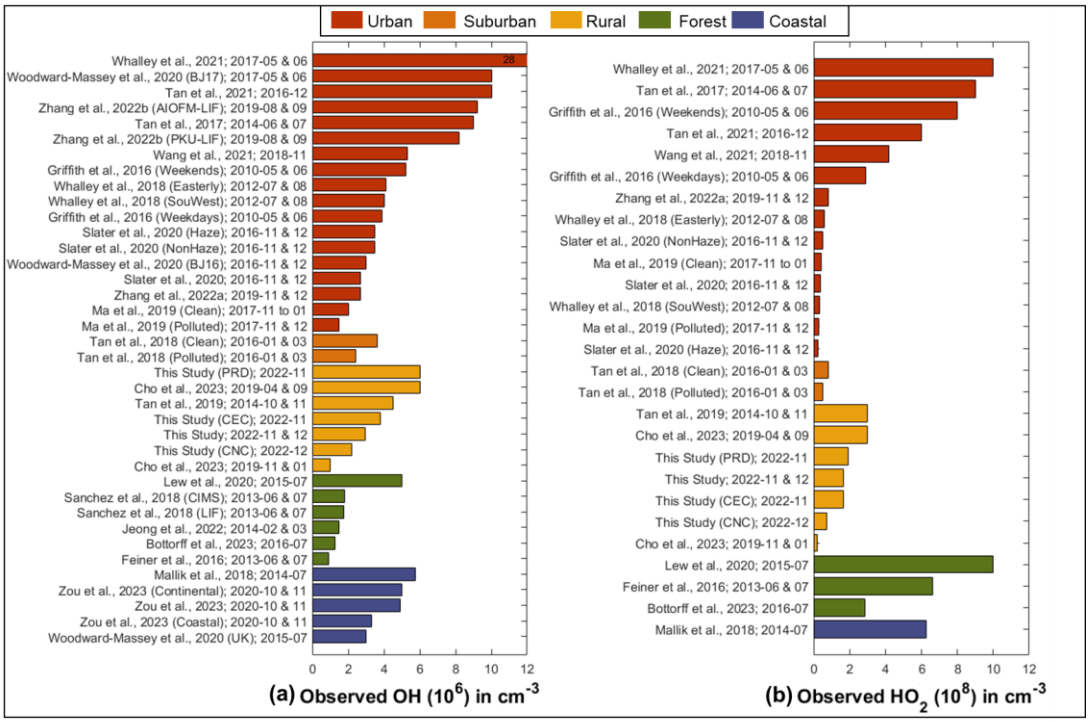

Figure S5 Typical daily averaged maximum concentration of (a) OH and (b) HO_2 observed in various geophysical regions, including coastal (blue), forest (green), rural (yellow) and urban (red).

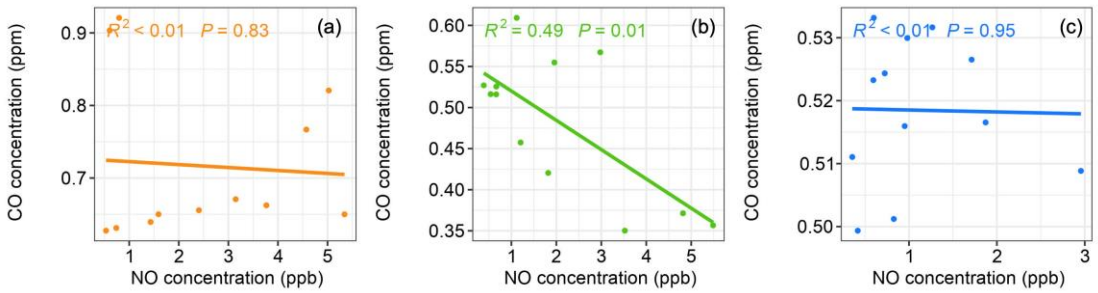

Figure S6 Relationship between NO and CO concentrations from 7:00 to 10:00 in (a) PRD, (b) CEC and (c) CNC. The solid lines depict the linear regression fits, with the corresponding equations R^2 and p-values annotated on the plot.

Table S1 The HO_X related reactions in the model.

Ambient: HO_x Productions	
(R1)	$O_3 + h\nu(<340\ nm) \rightarrow O(^1D) + O_2$
(R2)	$O(^1D) + H_2O \rightarrow OH + OH$
(R3)	Alkenes + $O_3 \rightarrow RO_X$ + Products
(R4)	$HONO + h\nu(<400\ nm) \rightarrow OH + NO$
(R5)	$HCHO + h\nu\ (<335\ nm) + 2O_2 \rightarrow 2HO_2 + CO$
Ambient: HO_x Interconvertions	
(R6)	$OH + RH + O_2 \rightarrow RO_2 + H_2O$
(R7)	$HCHO + OH + O_2 \rightarrow CO + H_2O + HO_2$
(R8)	$CO + OH + O_2 \rightarrow CO_2 + HO_2$
(R9)	$RO_2 + NO \rightarrow RO + NO_2$
(R10)	$RO + O_2 \rightarrow R'CHO + HO_2$
(R11)	$HO_2 + NO \rightarrow OH + NO_2$
(R12)	$HO_2 + O_3 \rightarrow OH + 2O_2$
(R13)	$NO_2 + h\nu(<420\ nm) + O_2 \rightarrow NO + O_3$
Ambient: HO_x Loss	
(R14)	$OH + NO_2 \rightarrow HNO_3$
(R15)	$OH + NO \rightarrow HONO$
(R16)	$RO_2 + NO \rightarrow RONO_2$
(R17)	$RO_2 + RO_2 \rightarrow$ products
(R18)	$RO_2 + HO_2 \rightarrow ROOH + O_2$
(R19)	$HO_2 + HO_2 \rightarrow H_2O_2 + O_2$
(R20)	$HO_2 + HO_2 + H_2O \rightarrow H_2O_2 + H_2O + O_2$
(R21)	$OH + SO_2 + O_2 + H_2O + M \rightarrow H_2SO_4 + HO_2 + M$
CIMS: Reactions in Sample Inlet System	
(R21)	$OH + SO_2 + O_2 + H_2O + M \rightarrow H_2SO_4 + HO_2 + M$
(R11)	$HO_2 + NO \rightarrow OH + NO_2$
(R22)	$RO_2 + NO + O_2 \rightarrow R'CHO + HO_2 + NO_2$
(R23)	Scavenger gas + $OH \rightarrow$ Products
CIMS: Reactions in Ionization Chamber	
(R24)	$HNO_3 + e^- \rightarrow NO_2^- + OH$
(R25)	$HNO_3 + NO_2^- \rightarrow NO_3^- + HONO$
(R26)	$NO_3^- + (HNO_3)_m + (H_2O)_n + M \rightarrow NO_3^-\cdot(HNO_3)_m\cdot(H_2O)_n + M$
(R27)	$H_2SO_4 + NO_3^-\cdot(HNO_3)_m\cdot(H_2O)_n \rightarrow HSO_4^-\cdot(HNO_3)_m(H_2O)_n + HNO_3$
CIMS: Reactions in Collisional Dissociation Chamber	
(R28)	$NO_3^-\cdot(HNO_3)_m\cdot(H_2O)_n + M \rightarrow NO_3^- + (HNO_3)_m + (H_2O)_n + M$
(R29)	$HSO_4^-\cdot(HNO_3)_m\cdot(H_2O)_n + M \rightarrow HSO_4^- + (HNO_3)_m + (H_2O)_n + M$
CIMS: Calibration	
(R30)	$H_2O + h\nu(184.9nm) + O_2 \rightarrow HO_2 + OH$

Table S2 Summary of instruments used, and species measured during the field campaign.

Instruments	Species	Resolution	Detection Limits	Accuracy
Q-CIMS (NO_3^-)	OH	1 hours	3×10^5 cm^{-3}	± 46%
	HO_2*	1 hours	20×10^5 cm^{-3}	± 44%
Thermo 42i-TL	NO	1 min	60 ppt	± 5.2%
Thermo 49i	O_3	1 min	1 ppb	± 6.0%
NO_2-11r-EP	NO_2	1 min	60 ppt	± 6.0%
Online GC-MS	VOCs	1 hour	10 ppt	± 20%
Thermo 43i	SO_2	1 min	0.5 ppb	± 6.1%
Thermo 48i	CO	1 min	40 ppb	± 7.4%
Thermo 17i	NH_3	2 mins	1 ppb	± 8%
LOPAP-03	HONO	5 mins	1 ppt	± 10%
SMPS	Aerosol Particles	5 mins	1 particle cm^{-3}	± 10%

1

Tabel S3 Configurations of the PolyU CIMS in Hok Tsui 2020 and Conghua 2022 campaigns. The changes from the last configuration were labelled by red color.

a) Hok Tsui 2020

Efficiency Related	Parameters	Gas	Values	Units	Specification for Measurement	Values	Units
E_{Conv}	**Front Injection**	SO_2 (0.9%)	5	sccm	Sample Flow [SO_2]	12	ppm
	Pulse Valve	N_2	2	sccm	Cycle Duration (OH)	6	mins
		C_3F_6 (99.9%)	2	sccm	B/S Ratio for OH measurement	8%	
	Rear Injection	C_3F_6 (99.9%)	2	sccm	Sample Flow [C_3F_6]	1072	ppm
		HNO_3	10	sccm	Reaction Time	47	ms
	Sample Flow		3.7	slpm	Sample Flow Speed	55	cm/s
E_{Ion}	**Sheath Flow**	Zero Air	12.6	slpm	Reynolds Number in Ionization Chamber	>4000 Turbulent flows	
		HNO_3	10	sccm			
		C_3F_6 (99.9%)	2	sccm	Sheath Flow [C_3F_6]	159	ppm
	Total Flow		16.8	slpm	Sheath Flow Speed	25	cm/s
	Sheath Voltages		-80	V	Voltages Difference for ionization	48	V
	Sample Voltages		-32	V			
E_{Trans}	**Buffer Gas**	N_2	440	sccm	Voltages Difference for transmission	80	V
	Buffer Voltages		-70	V			
	Pinhole Voltages		-40	V			
Cal	**Calibration Flow**		10	slpm	Calibration Factor C_{OH} (Reagent ion: $N^{18}O_3^-$)	$1.21*10^{-8}$	cm^3
	Flow Speed		65	cm/s			
	Product It Value		$8.8*10^{10}$	photon/cm^2			
Uncertainties		**Sigma**		2	**Detection Limit ($\times10^5$ cm^{-3}) (3σ)**	In lab	1.7
		Calibration		38%		Day	12
		Overall		44%		Night	8.5

b) CongHua 2022

Efficiency Related	Parameters	Gas	Values	Units	Specification for Measurement	Values	Units
E_{conv}	**Front Injection**	SO_2 (0.9%)	5	sccm	Sample Flow [SO_2]	12	ppm
		NO (0.9%)	0.5		Sample Flow [NO]	1.2	ppm
	Pulse Valve	N_2	2	sccm	Cycle Duration (OH)	6	mins
					Cycle Duration (HO_2)	60	mins
		C_3F_6 (99.9%)	2	sccm	B/S Ratio (OH)		10%
					B/S Ratio (HO_2)		20%
	Rear Injection	C_3F_6 (99.9%)	2	sccm	Sample Flow [C_3F_6]	1072	ppm
		HNO_3	10	sccm	Reaction Time	47	ms
	Sample Flow		3.7	slpm	Sample Flow Speed	55	cm/s
E_{Ion}	**Sheath Flow**	Zero Air	12.6	slpm	Reynolds Number in Ionization Chamber	>4000 Turbulent flows	
		HNO_3	10	sccm			
		C_3F_6 (99.9%)	2	sccm	Sheath Flow [C_3F_6]	159	ppm
	Total Flow		16.8	slpm	Sheath Flow Speed	25	cm/s
	Sheath Voltages		-80	V	Voltages Difference for ionization	48	V
	Sample Voltages		-32	V			
E_{Trans}	**Buffer Gas**	N_2	440	sccm	Voltages Difference for transmission	80	V
	Buffer Voltages		-70	V			
	Pinhole Voltages		-40	V			
Cal	**Calibration Flow**		10	slpm	Calibration Factors ($N^{18}O_3^-$)	C_{OH}	$1.09*10^{-8}$ cm^3
	Flow Speed		65	cm/s		C_{HO2}	$1.07*10^{-8}$
	Product It Value		$8.8*10^{10}$	photon/cm^2		C_{H2SO4}	$6.01*10^{-9}$
Overall Uncertainties (2σ)		OH		44%	**Detection Limit in Field Study ($\times10^5$ cm^{-3}) (3σ)**	OH	3
		H_2SO_4		40%		H_2SO_4	1
		HO_2		46%		HO_2	20

Notes: B/S Ratio - background to signal ratio.

Table S4 Average mixing ratios (ppbv) and standard deviations of measured VOCs that are constrained in the box model in the entire campaign and in different cases.

Species	Total	PRD	CEC	CNC	MCM Abb.
Ethane	2.301±0.826	1.613±0.883	1.864±0.534	2.032±0.141	C2H6
Ethylene	0.691±0.331	0.622±0.257	0.582±0.206	0.581±0.162	C2H4
Propane	1.593±0.618	2.099±0.808	1.217±0.314	1.239±0.274	C3H8
Propene	0.072±0.077	0.127±0.173	0.059±0.023	0.067±0.035	C3H6
i-Butane	0.439±0.281	0.891±0.494	0.353±0.103	0.310±0.061	IC4H10
n-Butane	0.653±0.405	1.284±0.709	0.484±0.145	0.438±0.083	NC4H10
Acetylene	0.917±0.416	0.905±0.350	0.819±0.305	0.758±0.072	C2H2
trans-2-Butene	0.015±0.007	0.015±0.005	0.017±0.011	0.016±0.006	TBUT2ENE
cis-2-Butene	0.083±0.038	0.165±0.033	0.083±0.013	0.080±0.014	CBUT2ENE
Butene	0.044±0.021	0.047±0.049	0.037±0.014	0.048±0.010	BUT1ENE
Chloromethane	0.838±0.221	0.510±0.076	0.839±0.153	0.856±0.154	CH3CL
1,3-Butadiene	0.008±0.008	0.012±0.009	0.008±0.007	0.007±0.005	C4H6
Acetaldehyde	0.922±0.355	1.456±0.365	NaN	0.525±0.160	CH3CHO
Bromomethane	0.009±0.002	0.010±0.002	0.009±0.001	0.009±0.001	CH3BR
Chloroethane	0.023±0.012	0.015±0.011	0.021±0.009	0.020±0.004	CH3CH2CL
i-Pentane	0.338±0.167	0.610±0.224	0.311±0.059	0.237±0.042	IC5H12
1-Pentene	0.043±0.016	0.067±0.024	0.033±0.008	0.037±0.006	PENT1ENE
n-Pentane	0.187±0.102	0.339±0.181	0.121±0.034	0.136±0.022	NC5H12
trans-2-Pentene	0.003±0.005	0.011±0.005	0.002±0.002	0.001±0.001	TPENT2ENE
cis-2-Pentene	0.002±0.003	0.007±0.003	0.001±0.001	0.000±0.001	CPENT2ENE
Acrolein	0.060±0.031	0.092±0.043	0.053±0.019	0.043±0.015	ACR
Propanal	0.011±0.006	0.015±0.011	0.010±0.004	0.009±0.004	C2H5CHO
Vinylidene chloride	0.004±0.003	0.003±0.002	0.002±0.002	0.005±0.003	CCL2CH2
2,2-Dimethylbutane	0.017±0.015	0.046±0.025	0.012±0.003	0.010±0.002	M22C4
Dichloromethane	1.142±0.838	2.510±1.430	1.035±0.347	0.933±0.179	CH2CL2
2,3-Dimethylbutane	0.026±0.023	0.064±0.033	0.025±0.007	0.015±0.004	M23C4
2-Methylpentane	0.071±0.045	0.237±0.053	0.060±0.016	0.056±0.012	M2PE
3-Methylpentane	0.052±0.039	0.120±0.061	0.040±0.011	0.036±0.009	M3PE
Methyl tert-butyl ether	0.072±0.042	0.135±0.051	0.068±0.016	0.055±0.012	MTBE
1-Hexene	0.005±0.005	0.013±0.004	0.004±0.004	0.002±0.001	HEX1ENE
n-Hexane	0.066±0.043	0.131±0.063	0.049±0.016	0.042±0.012	NC6H14
Methacrolein	0.062±0.062	0.116±0.058	0.108±0.069	0.025±0.010	MACR
1,1-Dichloroethane	0.009±0.005	0.008±0.004	0.008±0.004	0.007±0.001	CHCL2CH3
Butyraldehyde	0.536±0.211	0.446±0.179	0.496±0.142	0.448±0.157	C3H7CHO
1,2-Dichloroethylene	0.049±0.076	0.138±0.171	0.032±0.014	0.026±0.014	DICLETH
2-Butanone	0.248±0.244	0.546±0.490	0.214±0.086	0.134±0.050	MEK
Ethyl acetate	0.267±0.386	0.707±0.868	0.174±0.076	0.148±0.076	ETHACET
Chloroform	0.082±0.032	0.125±0.042	0.087±0.015	0.069±0.010	CHCL3
Methylchloroform	0.002±0.001	0.004±0.000	0.001±0.000	0.002±0.000	CH3CCL3
2-Methylhexane	0.015±0.017	0.046±0.028	0.010±0.004	0.007±0.002	M2HEX
Cyclohexane	0.019±0.015	0.041±0.021	0.011±0.005	0.011±0.004	CHEX
Tetrachloromethane	0.073±0.006	0.070±0.004	0.066±0.004	0.075±0.003	CCL4
3-Methylhexane	0.020±0.024	0.064±0.042	0.012±0.004	0.009±0.003	M3HEX
Benzene	0.346±0.139	0.288±0.106	0.315±0.102	0.311±0.029	BENZENE
Ethylene dichloride	0.359±0.170	0.259±0.112	0.342±0.185	0.414±0.097	CH2CLCH2CL
n-Hepane	0.035±0.023	0.072±0.038	0.024±0.005	0.022±0.003	NC7H16
Crotonaldehyde	0.446±0.139	0.464±0.008	0.480±0.007	0.501±0.008	C3MDBAL
Trichloroethene	0.021±0.023	0.061±0.037	0.018±0.013	0.013±0.003	TRICLETH
1,2-Dichloropropane	0.085±0.038	0.118±0.030	0.096±0.016	0.071±0.011	CL12PROP
Pantanal	0.018±0.011	0.033±0.017	0.019±0.008	0.013±0.006	C4H9CHO
1,3-Dichloro-1-propene	0.003±0.001	0.003±0.001	0.002±0.001	0.002±0.001	CLC3H4CL
4-Methyl-2-pentanone	0.005±0.007	0.019±0.004	0.001±0.001	0.000±0.001	MIBK
Toluene	0.282±0.266	0.706±0.498	0.212±0.057	0.173±0.049	TOLUENE
n-Octane	0.009±0.007	0.022±0.007	0.005±0.001	0.005±0.001	NC8H18
1,1,2-Trichloroethane	0.014±0.010	0.011±0.008	0.013±0.009	0.015±0.005	CH2CLCHCL2
Tetrachloroethylene	0.015±0.013	0.040±0.019	0.014±0.004	0.009±0.001	TCE
2-Hexanone	0.050±0.025	0.087±0.029	NaN	0.038±0.011	HEX2ONE
Hexanal	0.041±0.022	0.076±0.025	NaN	0.030±0.009	C5H11CHO
1,2-Dibromoethane	0.002±0.002	0.004±0.001	0.001±0.001	0.002±0.001	DIBRET
Ethylbenzene	0.042±0.031	0.072±0.035	0.028±0.022	0.034±0.023	EBENZ
o-Xylene	0.039±0.030	0.077±0.039	0.027±0.018	0.031±0.017	OXYL
Styrene	0.020±0.013	0.034±0.008	0.012±0.005	0.013±0.007	STYRENE
Isopropylbenzene	0.006±0.006	0.016±0.003	0.003±0.001	0.003±0.001	IPBENZ
1,1,2,2-Tetrachloroethane	0.003±0.002	0.005±0.001	0.003±0.002	0.002±0.001	CHCL2CHCL2
n-Propylbenzene	0.005±0.004	0.013±0.003	0.003±0.001	0.002±0.001	PBENZ
m-Ethyltoluene	0.007±0.007	0.019±0.008	0.006±0.003	0.004±0.002	METHTOL
p-Ethyltoluene	0.005±0.005	0.013±0.005	0.003±0.002	0.002±0.002	PETHTOL
1,3,5-Trimethylbenzene	0.005±0.005	0.015±0.005	0.004±0.002	0.002±0.001	TM135B
n-Decane	0.003±0.003	0.009±0.003	0.002±0.001	0.001±0.001	NC10H22
Benzaldehyde	0.005±0.004	0.013±0.004	0.003±0.001	0.002±0.001	BENZAL
1,2,4-Trimethylbenzene	0.009±0.009	0.024±0.013	0.008±0.003	0.004±0.002	TM124B
1,2,3-Trimethylbenzene	0.004±0.003	0.010±0.004	0.003±0.002	0.002±0.001	TM123B
Undecane	0.002±0.002	0.006±0.001	0.002±0.001	0.000±0.001	NC11H24
Dodecane	0.009±0.003	0.015±0.003	0.007±0.001	0.010±0.002	NC12H26

Text S1 Calibration procedures

The calibration of the Chemical Ionization Mass Spectrometer (CIMS) involves the generation of OH and HO_2 radicals through photolysis of water vapor by 184.9 nm light, as outlined in Reaction R30. The concentration of radicals produced during calibration is determined from the known concentration of water vapor [H_2O], which is calculated from water vapor pressure, the relative humidity and temperature. Other essential parameters include the photolysis cross-section of water vapor (σ_{H2O} = 7.14 × 10^{-20} cm^2; Cantrell et al., 1997), the photolysis quantum yield (Φ, assumed to be 1, Kürten et al., 2012) and the photon flux (*It* value, see details about *It* value determination on Kürten et al., 2012). The generated radical concentrations ([OH] and [HO_2]) are calculated using the following equation:

$$[OH] = [HO_2] = [H_2O] * \sigma_{H_2O} * \Phi * It$$

From these values, the calibration factors for OH and HO_2 (C_{OH} and C_{HO2}) are calculated using the signals obtained during calibration (S_{OHcal} and S_{HO2cal}), as expressed in the transformed form of Equations E1 and E2:

$$C_{OH} = \frac{1}{[OH]_{cal}} \times \frac{S_{OHcal}}{S_{62}} \text{ (E1, transformed)}$$

$$C_{HO2} = \frac{1}{[HO_2]_{cal}} \times \frac{S_{HO2cal}}{S_{62}} \text{ (E2, transformed)}$$

The calibrator produced OH and HO_2 concentrations in the range of 3 × 10^7 to 1 × 10^9 cm^{-3} depending on RH conditions in 10 LMP synthetic air. More detailed information on calculation procedures is given in our previous study (Zou et al., 2023).

Text S2 Modification for HO_2 measurement

To measure HO_2, a valve was added to switch the injection gas between NO and N_2 as indicated by the purple frame in Figure S2. When N_2 is added, the CIMS operates in OH measurement mode. When NO is added to the sample flow, the CIMS switches to HO_2 mode for total HO_x measurement.

During HO_2 measurement, ambient HO_2 is converted by NO to OH. It should be noted that in HO_2 mode, the increasing NO concentration can enhance HO_2 conversion to OH (R11). However, excessive NO levels trigger the HONO formation

when reacts with OH (R15), competing with the OH conversion process by SO_2 (R21) and lowering the detection efficiency for OH. Consequently, the NO-to-SO_2 concentration ratio is crucial for HO_2 measurements. Sensitivity tests revealed an optimal [NO]/[SO_2] ratio of 0.1 for the PolyU-CIMS, achieving 100% conversion of HO_2 in the laboratory ([H_2SO_4]/[HO_2] = 1), aligning with prior research recommendations (Edwards et al., 2003; Sjostedt et al., 2007). Because the concentrations of both SO_2 and NO injected into the sample flow are maintained at levels over 100-1000 times higher than ambient levels, and the injection flow rates are fixed, the efficiency of the HO_2-to-OH conversion remains stable and is believed to be complete.

Text S3 The Background mode and scavenge efficiency

In the background mode, the scavenger gas C_3F_6 is introduced into the sample flow along with SO_2. Since the concentration of C_3F_6 is 100 times higher than that of SO_2, ambient OH and any HO_2 converted to OH are scavenged by C_3F_6, rather than converted to H_2SO_4.

To determine the amount of C_3F_6 needed to achieve complete OH scavenging, we gradually increased the C_3F_6 concentration added to high levels of OH and HO_2 ([HO_x] $\approx 10^9$ cm^{-3}) generated from the calibrator in synthetic air until no further reduction in the measured signal, which indicates complete scavenging of OH. This point defines the background noise, which is attributed to any Criegee intermediates and ambient sulfuric acid. In our setup, residual C_3F_6 is present after the CIMS switches from background to signal mode, but it does not affect the measurement results. As shown in Figure S7, after switching off C_3F_6, the measurement signals rapidly return to their initial levels within 20 seconds. Data affected by residual C_3F_6 is excluded to minimize its impact on the measurements.

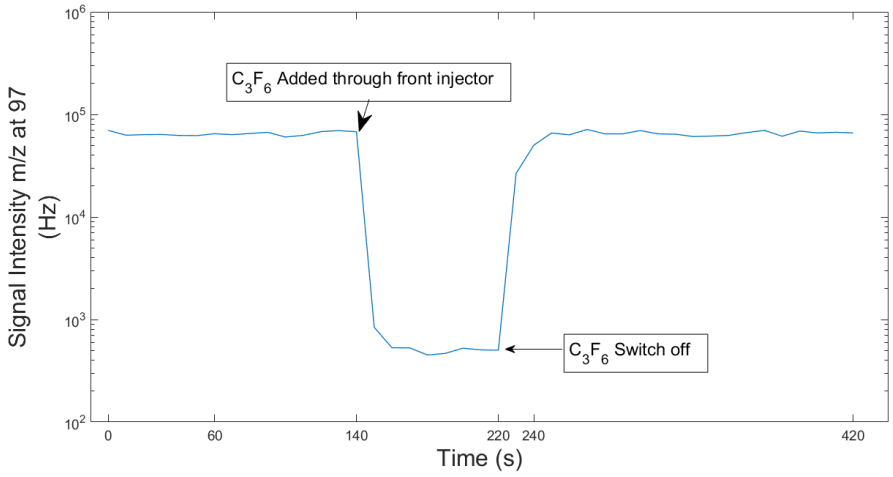

Figure S7 Variation of signal intensity m/z at 97 before C_3F_6 addition with time, after addition and switching off of C_3F_6 in synthetic air containing OH of ~5×10^8 cm^{-3}.

Text S4 Measurement interferences

4.1 Sampling Loss

Wall losses in the ambient inlet were evaluated by varying the distance between the calibration lamp and the inlet to assess potential signal attenuation. The instrument was calibrated in two distinct configurations: initially, the lamp was positioned close to the CIMS sample inlet (Figure S6a), and subsequently, moved away from the CIMS sample inlet (Figure S6b). By comparing the observed signals from these two configurations, we were able to calculate the wall losses associated with the ambient inlet. The results indicated no significant difference (<1%) between the two measurements, suggesting negligible wall losses in the sampling system.

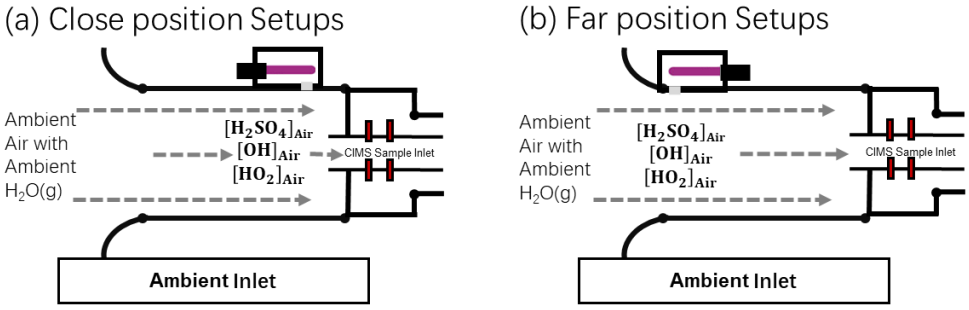

Figure S8 Calibration process during ambient sampling in (a) close and (b) far positions.

Furthermore, the potential for radical-radical loss after the radicals exit the calibrator and enter the sampling inlet was considered. Given the flow speed of the ambient inlet (12.2 m/s) the sample inlet (55 cm/s), along with the short distances involved—the calibration lamp is less than 1 cm from the sample inlet, and the sampling port to the front injectors is 1 cm—the calculated transport time for radicals to reach the front injectors is less than 20 ms. This short transport time is sufficiently short to prevent significant radical-radical losses. Additionally, since the sample inlet draws from the central part of the airflow within the ambient inlet, and the flow is laminar, wall losses at this stage are also considered negligible.

4.2 OH interference

The OH interference in the PolyU-CIMS, resulting from ambient NO + HO_2 recycling (R11) and ionization process (R24, artificial OH), was accounted for and included in the measurement uncertainty, as outlined by Zou et al. (2023). To assess and correct this interference, model simulations were conducted. Initially, we constrained all measured species (except OH) in the model, and a three-day spin-up was used to simulate the chemical conditions of the sampled air during measurement. Subsequently, the outputs (except OH) were utilized as inputs for another simulation that included the injection of 12 ppm SO_2, to simulate chemical reactions in the inlet with reaction time of 47 ms - matching the reaction time in the CIMS. Photolysis frequencies were maintained at zero to simulate the dark environment of the inlet. The modeled H_2SO_4 concentrations reflect interference from NO + HO_2 reactions, with an average value of 2.91×10^4 and range from 10^4 to 10^5 cm^{-3} throughout the whole campaign. These calculated interferences were subtracted from the ambient results.

In this study, the PolyU-CIMS encountered additional interference from residual NO in the injectors when switching from NO (used for HO_2 measurement) to N_2 (used for OH measurement). To prevent residual NO buildup, the inlet was cleaned daily, and a one-hour calibration was performed at both the start and end of day's measurements to monitor NO residuals. Monitoring results showed that the NO residual time for the PolyU - CIMS was approximately 26 mins, similar to values

reported in earlier studies (Edwards et al., 2003; Sjostedt et al., 2007). Consequently, data collected during the residual period (30 mins after switching the measurement target from HO_2 to OH) were discarded to eliminate NO residual interference from the final dataset. Details about how the duty cycle was configured to monitor NO residual interference are provided in Text S5.

4.3 HO_2 interference

The concentration of injected NO is the primary source of HO_2 measurement interference in this study. High NO concentrations convert ambient RO_2, particularly alkene and aromatic-related RO_2, into HO_2 and then OH, leading to a positive bias in HO_2 measurements (Fuchs et al., 2014). To assess HO_2 interference, we conducted model analysis using the same settings as those used for OH interference, including observational data input (except HO_2* and OH), reaction time, and dark conditions, while adjusting specific parameters to address HO_2-related reactions. The modeled ambient RO_2 concentrations (blue line in Figure S9a) were used as inputs for additional simulations assessing RO_2 interference with HO_2 via reaction with added NO (1.2 ppm) and SO_2 (12 ppm) in the CIMS inlet. The H_2SO_4 concentrations resulting from the model simulation represent the interference in HO_2 measurements attributed to RO_2 (blue line in Figure S9b). By comparing these results with the modeled H_2SO_4 concentrations (red line in Figure S9b) when modelled ambient HO_2 concentrations (red line in Figure S9a) are constrained, we determine that the modelled average daytime (08:00-16:00) RO_2 interference increased HO_2 by 127%, 117%, and 144% PRD, CEC and CNC case, respectively, and in ranged of 79% to 222% throughout the campaign. These results indicate substantial positive interference from RO_2 in HO_2 measurements under the CIMS configurations adopted in the field study.

We note that the MCM model has inherent uncertainties on RO_2 chemistry, such as incomplete representations of RO_2 species and the assumption that most of RO_2 species share the same reaction rate constant with NO. In addition, HO_2 was over-

simulated by the model (Figure S9a). For these reasons, we use the modeled interferences only for sensitivity tests and qualitative discussion rather than correcting the measured HO_2*. Nonetheless, these values indicate the potential magnitude of positive interference in HO_2* measurements caused by RO_2.

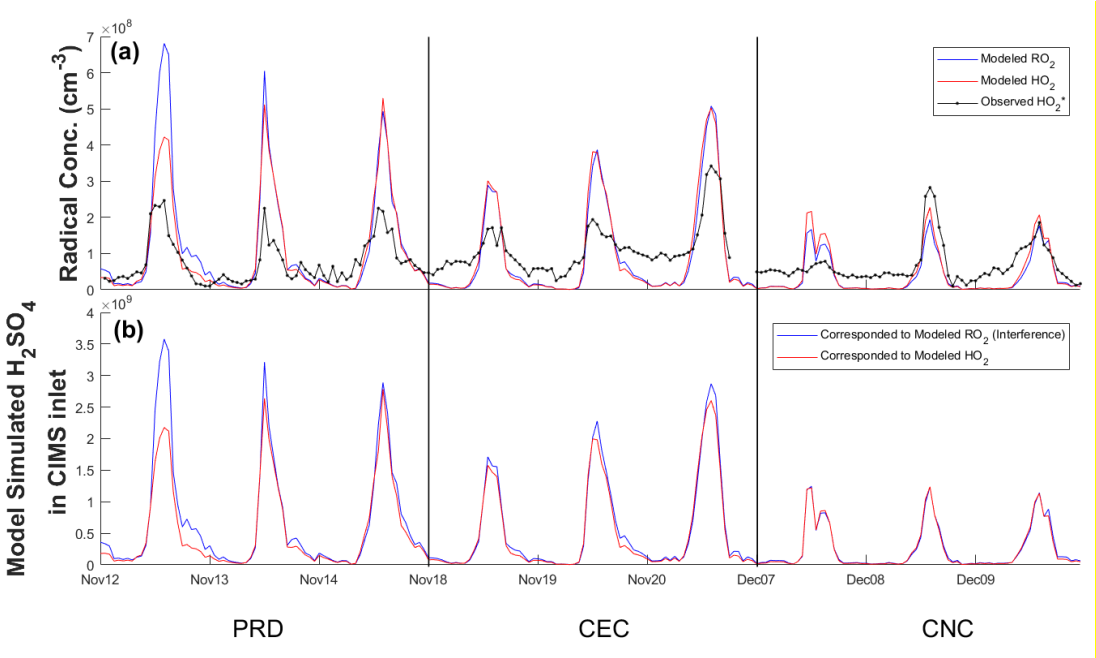

Figure S9: Modeled peroxyl radical concentrations and resulting H_2SO_4 simulations. (a) Temporal profiles of modeled RO_2 and HO_2 concentrations alongside observed HO_2* for the PRD, CEC, and CNC periods. (b) Simulated H_2SO_4 concentrations corresponding to RO_2 and HO_2 in the CIMS inlet for the same periods.

Text S5 The measurement duty cycle of CIMS

As detailed in Section 2.2, the PolyU-CIMS was configured to sequentially measure HO_2, H_2SO_4, and OH within each hour during the field study, corresponding to changes in the injection gases. Table S3 outlines the hourly measurement schedule and associated injection gases, while Figure S10 illustrates the 1-hour duty cycle.

Table S5 Duty cycle and injection gases for targeted chemical analysis.

Purpose	Measurement Mode	Signal 97 Label	Chemicals injected to the sample flow through different injectors		Duty time (s)	Repeat times	Total Duration (mins)
			Front Injectors	Rear Injectors			
HO_2*	SIG	S_{97NO}	NO, $N_{2(p)}$, SO_2,	Sca, $Sca_{(p)}$	60	3	6
	BKG	$S_{97NOSca}$	NO, $Sca_{(p)}$, SO_2	Sca, $N_{2(p)}$	60		
H_2SO_4	SIG	$S_{97w/o}$	-	Sca, $Sca_{(p)}$	60	2	4
	BKG	$S_{97w/o}$	-	Sca, $N_{2(p)}$	60		
OH	SIG	S_{97SO2}	$N_{2(p)}$, SO_2,	Sca, $Sca_{(p)}$	60	3	50
	BKG	$S_{97SO2Sca}$	$Sca_{(p)}$, SO_2	Sca, $N_{2(p)}$	60		

Notes:

Front and Rear Injectors - The injector pairs as demonstrated in Figure S2

SIG & BKG – the signal and background modes.

Sca - scavenger gas, C_3F_6 in this study.

$Sca_{(p)}$ - scavenger gas added through the pulsed flow.

$N_{2(p)}$- nitrogen gas, added through the pulsed flow.

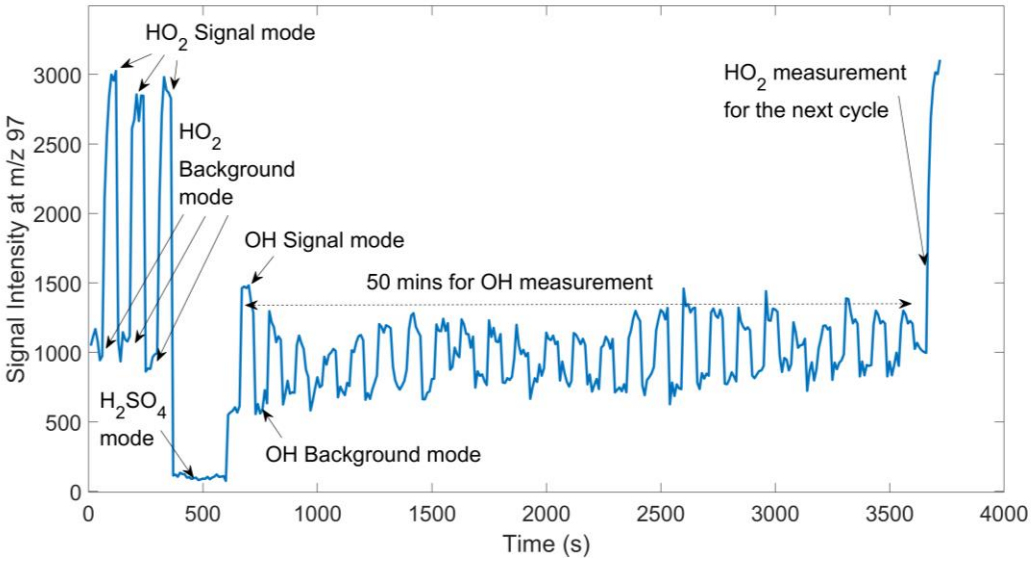

Figure S10 Variation of signal intensity at m/z 97 during a 1-hour duty cycle of CIMS measurement.

Reference

Bottorff, B., Lew, M. M., Woo, Y., Rickly, P., Rollings, M. D., Deming, B., Anderson,

D. C., Wood, E., Alwe, H. D., Millet, D. B., Weinheimer, A., Tyndall, G., Ortega, J., Dusanter, S., Leonardis, T., Flynn, J., Erickson, M., Alvarez, S., Rivera-Rios, J. C., Shutter, J. D., Keutsch, F., Helmig, D., Wang, W., Allen, H. M., Slade, J. H., Shepson, P. B., Bertman, S., and Stevens, P. S.: OH, HO_2, and RO_2 radical chemistry in a rural forest environment: measurements, model comparisons, and evidence of a missing radical sink, Atmospheric Chemistry and Physics, 23, 10287–10311, https://doi.org/10.5194/acp-23-10287-2023, 2023.

Cho, C., Fuchs, H., Hofzumahaus, A., Holland, F., Bloss, W. J., Bohn, B., Dorn, H.-P., Glowania, M., Hohaus, T., Liu, L., Monks, P. S., Niether, D., Rohrer, F., Sommariva, R., Tan, Z., Tillmann, R., Kiendler-Scharr, A., Wahner, A., and Novelli, A.: Experimental chemical budgets of OH, HO_2, and RO_2 radicals in rural air in western Germany during the JULIAC campaign 2019, Atmospheric Chemistry and Physics, 23, 2003–2033, https://doi.org/10.5194/acp-23-2003-2023, 2023.

Edwards, G. D., Cantrell, C. A., Stephens, S., Hill, B., Goyea, O., Shetter, R. E., Mauldin, R. L., Kosciuch, E., Tanner, D. J., and Eisele, F. L.: Chemical Ionization Mass Spectrometer Instrument for the Measurement of Tropospheric HO_2 and RO_2, Anal. Chem., 75, 5317–5327, https://doi.org/10.1021/ac034402b, 2003.

Feiner, P. A., Brune, W. H., Miller, D. O., Zhang, L., Cohen, R. C., Romer, P. S., Goldstein, A. H., Keutsch, F. N., Skog, K. M., Wennberg, P. O., Nguyen, T. B., Teng, A. P., DeGouw, J., Koss, A., Wild, R. J., Brown, S. S., Guenther, A., Edgerton, E., Baumann, K., and Fry, J. L.: Testing Atmospheric Oxidation in an Alabama Forest, Journal of the Atmospheric Sciences, 73, 4699–4710, https://doi.org/10.1175/JAS-D-16-0044.1, 2016.

Fuchs, H., Acir, I.-H., Bohn, B., Brauers, T., Dorn, H.-P., Häseler, R., Hofzumahaus, A., Holland, F., Kaminski, M., Li, X., Lu, K., Lutz, A., Nehr, S., Rohrer, F., Tillmann, R., Wegener, R., and Wahner, A.: OH regeneration from methacrolein oxidation investigated in the atmosphere simulation chamber SAPHIR, Atmos. Chem. Phys., 14, 7895–7908, https://doi.org/10.5194/acp-14-7895-2014, 2014.

Griffith, S. M., Hansen, R. F., Dusanter, S., Michoud, V., Gilman, J. B., Kuster, W. C., Veres, P. R., Graus, M., Gouw, J. A., Roberts, J., Young, C., Washenfelder, R., Brown, S. S., Thalman, R., Waxman, E., Volkamer, R., Tsai, C., Stutz, J., Flynn, J. H., Grossberg, N., Lefer, B., Alvarez, S. L., Rappenglueck, B., Mielke, L. H., Osthoff, H. D., and Stevens, P. S.: Measurements of hydroxyl and hydroperoxy radicals during CalNex-LA: Model comparisons and radical budgets, J. Geophys. Res. Atmos., 121, 4211–4232, https://doi.org/10.1002/2015JD024358, 2016.

Jeong, D., Seco, R., Emmons, L., Schwantes, R., Liu, Y., McKinney, K. A., Martin, S. T., Keutsch, F. N., Gu, D., Guenther, A. B., Vega, O., Tota, J., Souza, R. A. F., Springston, S. R., Watson, T. B., and Kim, S.: Reconciling Observed and Predicted Tropical Rainforest OH Concentrations, JGR Atmospheres, 127, https://doi.org/10.1029/2020JD032901, 2022.

Lew, M. M., Rickly, P. S., Bottorff, B. P., Reidy, E., Sklaveniti, S., Léonardis, T., Locoge, N., Dusanter, S., Kundu, S., Wood, E., and Stevens, P. S.: OH and HO_2 radical chemistry in a midlatitude forest: measurements and model comparisons, Atmospheric Chemistry and Physics, 20, 9209–9230, https://doi.org/10.5194/acp-20-9209-2020, 2020.

Ma, X., Tan, Z., Lu, K., Yang, X., Liu, Y., Li, S., Li, X., Chen, S., Novelli, A., Cho, C., Zeng, L., Wahner, A., and Zhang, Y.: Winter photochemistry in Beijing: Observation and model simulation of OH and HO2 radicals at an urban site, Science of The Total Environment, 685, 85–95, https://doi.org/10.1016/j.scitotenv.2019.05.329, 2019.

Mallik, C., Tomsche, L., Bourtsoukidis, E., Crowley, J. N., Derstroff, B., Fischer, H., Hafermann, S., Hüser, I., Javed, U., Keßel, S., Lelieveld, J., Martinez, M., Meusel, H., Novelli, A., Phillips, G. J., Pozzer, A., Reiffs, A., Sander, R., Taraborrelli, D., Sauvage, C., Schuladen, J., Su, H., Williams, J., and Harder, H.: Oxidation processes in the eastern Mediterranean atmosphere: evidence from the modelling of HO_x measurements over Cyprus, Atmospheric Chemistry and Physics, 18, 10825–10847, https://doi.org/10.5194/acp-18-10825-2018, 2018.

Mo, Z., Shao, M., and Lu, S.: Compilation of a source profile database for hydrocarbon

and OVOC emissions in China, Atmos. Environ., 143, 209–217, https://doi.org/10.1016/j.atmosenv.2016.08.025, 2016.

Sanchez, D., Jeong, D., Seco, R., Wrangham, I., Park, J.-H., Brune, W. H., Koss, A., Gilman, J., de Gouw, J., Misztal, P., Goldstein, A., Baumann, K., Wennberg, P. O., Keutsch, F. N., Guenther, A., and Kim, S.: Intercomparison of OH and OH reactivity measurements in a high isoprene and low NO environment during the Southern Oxidant and Aerosol Study (SOAS), Atmospheric Environment, 174, 227–236, https://doi.org/10.1016/j.atmosenv.2017.10.056, 2018.

Sjostedt, S. J., Huey, L. G., Tanner, D. J., Peischl, J., Chen, G., Dibb, J. E., Lefer, B., Hutterli, M. A., Beyersdorf, A. J., Blake, N. J., Blake, D. R., Sueper, D., Ryerson, T., Burkhart, J., and Stohl, A.: Observations of hydroxyl and the sum of peroxy radicals at Summit, Greenland during summer 2003, Atmospheric Environment, 41, 5122–5137, https://doi.org/10.1016/j.atmosenv.2006.06.065, 2007.

Slater, E. J., Whalley, L. K., Woodward-Massey, R., Ye, C., Lee, J. D., Squires, F., Hopkins, J. R., Dunmore, R. E., Shaw, M., Hamilton, J. F., Lewis, A. C., Crilley, L. R., Kramer, L., Bloss, W., Vu, T., Sun, Y., Xu, W., Yue, S., Ren, L., Acton, W. J. F., Hewitt, C. N., Wang, X., Fu, P., and Heard, D. E.: Elevated levels of OH observed in haze events during wintertime in central Beijing, Atmospheric Chemistry and Physics, 20, 14847–14871, https://doi.org/10.5194/acp-20-14847-2020, 2020.

Tan, Z., Fuchs, H., Lu, K., Hofzumahaus, A., Bohn, B., Broch, S., Dong, H., Gomm, S., Häseler, R., He, L., Holland, F., Li, X., Liu, Y., Lu, S., Rohrer, F., Shao, M., Wang, B., Wang, M., Wu, Y., Zeng, L., Zhang, Y., Wahner, A., and Zhang, Y.: Radical chemistry at a rural site (Wangdu) in the North China Plain: observation and model calculations of OH, HO_2 and RO_2 radicals, Atmospheric Chemistry and Physics, 17, 663–690, https://doi.org/10.5194/acp-17-663-2017, 2017.

Tan, Z., Rohrer, F., Lu, K., Ma, X., Bohn, B., Broch, S., Dong, H., Fuchs, H., Gkatzelis, G. I., Hofzumahaus, A., Holland, F., Li, X., Liu, Y., Liu, Y., Novelli, A., Shao, M., Wang,

H., Wu, Y., Zeng, L., Hu, M., Kiendler-Scharr, A., Wahner, A., and Zhang, Y.: Wintertime photochemistry in Beijing: observations of RO_x radical concentrations in the North China Plain during the BEST-ONE campaign, Atmospheric Chemistry and Physics, 18, 12391–12411, https://doi.org/10.5194/acp-18-12391-2018, 2018.

Tan, Z., Lu, K., Jiang, M., Su, R., Wang, H., Lou, S., Fu, Q., Zhai, C., Tan, Q., Yue, D., Chen, D., Wang, Z., Xie, S., Zeng, L., and Zhang, Y.: Daytime atmospheric oxidation capacity in four Chinese megacities during the photochemically polluted season: a case study based on box model simulation, Atmos. Chem. Phys., 19, 3493–3513, https://doi.org/10.5194/acp-19-3493-2019, 2019.

Tan, Z., Ma, X., Lu, K., Jiang, M., Zou, Q., Wang, H., Zeng, L., and Zhang, Y.: Direct evidence of local photochemical production driven ozone episode in Beijing: A case study, Science of The Total Environment, 800, 148868, https://doi.org/10.1016/j.scitotenv.2021.148868, 2021.

Wang, G., Iradukunda, Y., Shi, G., Sanga, P., Niu, X., and Wu, Z.: Hydroxyl, hydroperoxyl free radicals determination methods in atmosphere and troposphere, Journal of Environmental Sciences, 99, 324–335, https://doi.org/10.1016/j.jes.2020.06.038, 2021.

Whalley, L. K., Stone, D., Dunmore, R., Hamilton, J., Hopkins, J. R., Lee, J. D., Lewis, A. C., Williams, P., Kleffmann, J., Laufs, S., Woodward-Massey, R., and Heard, D. E.: Understanding in situ ozone production in the summertime through radical observations and modelling studies during the Clean air for London project (ClearfLo), Atmos. Chem. Phys., 18, 2547–2571, https://doi.org/10.5194/acp-18-2547-2018, 2018.

Whalley, L. K., Slater, E. J., Woodward-Massey, R., Ye, C., Lee, J. D., Squires, F., Hopkins, J. R., Dunmore, R. E., Shaw, M., Hamilton, J. F., Lewis, A. C., Mehra, A., Worrall, S. D., Bacak, A., Bannan, T. J., Coe, H., Percival, C. J., Ouyang, B., Jones, R. L., Crilley, L. R., Kramer, L. J., Bloss, W. J., Vu, T., Kotthaus, S., Grimmond, S., Sun, Y., Xu, W., Yue, S., Ren, L., Acton, W. J. F., Hewitt, C. N., Wang, X., Fu, P., and Heard, D. E.: Evaluating the sensitivity of radical chemistry and ozone formation to ambient

VOCs and NO_x in Beijing, Atmospheric Chemistry and Physics, 21, 2125–2147, https://doi.org/10.5194/acp-21-2125-2021, 2021.

Woodward-Massey, R., Slater, E. J., Alen, J., Ingham, T., Cryer, D. R., Stimpson, L. M., Ye, C., Seakins, P. W., Whalley, L. K., and Heard, D. E.: Implementation of a chemical background method for atmospheric OH measurements by laser-induced fluorescence: characterisation and observations from the UK and China, Atmospheric Measurement Techniques, 13, 3119–3146, https://doi.org/10.5194/amt-13-3119-2020, 2020.

Yang, X.: A Review of the Direct Measurement of Total OH Reactivity: Ambient Air and Vehicular Emission, Sustainability, 15, 16246, https://doi.org/10.3390/su152316246, 2023.

Yao, Z., Shen, X., Ye, Y., Cao, X., Jiang, X., Zhang, Y., and He, K.: On-road emission characteristics of VOCs from diesel trucks in Beijing, China, Atmos. Environ., 103, 87–93, https://doi.org/10.1016/j.atmosenv.2014.12.028, 2015.

Zhang, G., Hu, R., Xie, P., Lu, K., Lou, S., Liu, X., Li, X., Wang, F., Wang, Y., Yang, X., Cai, H., Wang, Y., and Liu, W.: Intercomparison of OH radical measurement in a complex atmosphere in Chengdu, China, Science of The Total Environment, 838, 155924, https://doi.org/10.1016/j.scitotenv.2022.155924, 2022a.

Zhang, G., Hu, R., Xie, P., Lou, S., Wang, F., Wang, Y., Qin, M., Li, X., Liu, X., Wang, Y., and Liu, W.: Observation and simulation of HO_x radicals in an urban area in Shanghai, China, Science of The Total Environment, 810, 152275, https://doi.org/10.1016/j.scitotenv.2021.152275, 2022b.

Zou, Z., Chen, Q., Xia, M., Yuan, Q., Chen, Y., Wang, Y., Xiong, E., Wang, Z., and Wang, T.: OH measurements in the coastal atmosphere of South China: possible missing OH sinks in aged air masses, Atmospheric Chemistry and Physics, 23, 7057–7074, https://doi.org/10.5194/acp-23-7057-2023, 2023.